Feasibility Studies of RADAR detection of Extensive Air Showers from Ultra-high Energy Cosmic Rays

von

Nils Scharf

Diplomarbeit in P H Y S I K

vorgelegt der

Fakultät für Mathematik, Informatik und Naturwissenschaften
der RWTH Aachen

im Februar 2008

angefertigt im

III. Physikalischen Institut A
Prof. Dr. Thomas Hebbeker

Erstgutachter und Betreuer
Prof. Thomas Hebbeker
III. Physikalisches Institut A
RWTH Aachen

Zweitgutachter
Prof. Martin Erdmann
III. Physikalisches Institut A
RWTH Aachen

Contents

List of Figures

Part I.
Introduction

The Earth's atmosphere is constantly hit by charged particles from outer space, so called Cosmic Rays. Up to now there are several open questions regarding Cosmic Rays:

- What sources and production mechanisms generate Cosmic Rays?
- What is the shape of the upper end of the Cosmic Ray energy spectrum?
- How do Cosmic Ray particles propagate?
- Which particles make up Cosmic Rays?

Cosmic Rays with the highest energies are so rare that they are not detectable directly. When such a Cosmic Ray particle hits the Earth's atmosphere, it generates a particle cascade that can be detected. Such a cascade is called an Extensive Air Shower (EAS). To gain knowledge on the Cosmic Ray Particle, one has to measure the properties of the EAS.

Today there are two established detection methods for the measurement of EAS. The first is the sampling of the secondary particles with particle detectors on the ground. The second is the measurement of fluorescence light generated when the secondary particles of the cascade excite nitrogen atoms of the air. The Pierre Auger Observatory uses both detection methods to study the Highest Energy Cosmic Rays with an energy above 10^{18} eV. The combined detection of an air shower is called hybrid detection.

Because both established detection concepts have limits, there is a constant search for new detection methods: Currently under development is the measurement of radio pulses generated by the charged particles in the EAS (see for example [1]). All these detection concepts measure electromagnetic radiation or particles generated by the EAS.

A somewhat different detection concept is the active probing of the EAS by RADAR. The idea that EAS should be detectable by RADAR was first presented in 1940 [2] and first experiments were proposed 20 years later [3][4]. Up to today there are no confirmed detections of EAS by RADAR.

A RADAR detector for extensive air showers would have a nearly 100% duty cycle and is sensible to the whole shower development. In addition a large volume is visible by such a detector. It combines the two positive aspects of the existing detection concepts, nearly 100% duty cycle and calorimetric measurements, and is a promising kind of research.

In order to understand the properties of RADAR detection for EAS one has to understand general RADAR principles. In this work we present measurements done with a simple setup on two signal classes comparable to EAS: airplanes and micro-meteors. The results of these measurements are used to give an overview on the hardware and software requirements needed for EAS detection by RADAR and the expected properties of such a setup.

Part II.
Physics of the Highest Energy Cosmic Rays

At the beginning of the 20th century it was measured that 10 to 20 ions per cubic centimeter and second were produced in the air. The first theory to explain this ionisation was the decay of radioactive elements in the upper Earth crust. In 1912 Victor Hess flew in a balloon to an altitude of 5 km to measure the penetration power of the ionising radiation. If the radiation would have been produced inside the Earth, the ionisation should decrease with larger altitudes. But instead of a decreasing ionisation with altitude the ionisation was strongly increasing. Hess concluded that "radiation [...] enters the atmosphere from above" [5]. That was the discovery of cosmic rays. The discovery of the coincident detection of cosmic ray particles in detectors separated by several meters in 1939 by Pierre Auger marked the discovery of extensive air showers [6]. He concluded that the registered particles were part of a particle cascade induced by the interaction of a primary cosmic ray particle with the Earth's atmosphere.

1. The Origin of Cosmic Rays

The sun produces most of the cosmic rays with lower energies. An upper limit for solar protons is around 1 GeV. Cosmic rays with higher kinetic energies are of extrasolar origin. The highest energy cosmic ray measured up to now had an energy of $3 \cdot 10^{20}\ eV$ [7]. It was measured by the Fly's Eye experiment. A thermal production mechanism for the whole energy range is not likely because of the energy spectrum of cosmic rays (see section 2.3). Today several classes of objects are considered possible cosmic ray sources:

- Stellar black holes
- Interplanetary and galactic magnetic fields
- White dwarfs or neutron stars
- Supernova remnants
- Several types of active galactic nuclei (AGN).

2. Acceleration of Cosmic Ray Particles

To explain the production of cosmic rays with the highest energies there are today two possible production scenarios:
The first is the so called bottom - up scenario: Particles with low energy are accelerated in the universe by classic acceleration mechanisms, for example electromagnetic acceleration for charged particles.
The second scenario is called top - down. It explains the highest energy cosmic rays as originating from the decay of very heavy exotic particles that are remnants of the big bang. When these exotic particles decay into standard model particles a high part of their mass energy is transfered into the kinetic energy of the standard model particle because of the relatively high mass of the decaying particle. The second mechanism relies on undiscovered physics therefore only the bottom - up scenario is explained below.

Todays favored acceleration mechanism for particle energies up to $10^{15}eV$ was first developed by Enrico Fermi [8]. It describes the acceleration of charged particles in turbulent magnetic fields by statistical scattering. These turbulent magnetic fields exist for example in plasma shock fronts. Plasma shock fronts can be built either by catastrophic events such as super nova explosions or as bow shocks of objects moving through a plasma medium. This principle was proven for the low energy regime by studies on the bow shock of the Earth in the solar wind and the bow shocks of other planets [9]. In [10] A.M. Hillas explains the properties and constrains of the Fermi mechanism:

The Lamor radius (or gyro radius) r_L in parsec[1], that is the radius of the circular motion inside a magnetic field with the component B in μG normal to the velocity of the particle, for a relativistic particle with charge $Z \cdot e$ and energy E is given by:

$$r_L = 1,08\ pc \cdot \frac{E}{10^{15}\ GeV} \cdot \frac{\mu G}{Z \cdot B} \tag{1}$$

For the acceleration in turbulent regions it follows that the size of the accelerating region L must be far greater than:

$$2 \cdot r_L \sim 2 \cdot \frac{E \cdot \mu G}{B \cdot 10^{15}\ eV} \tag{2}$$

otherwise the particle would leave the region before it could be accelerated to its energy E, the maximum energy possible in that region. This is modified by taking into account the velocity of scattering centers βc which then gives that L has to be larger than $2 \cdot r_L/\beta$:

$$B \cdot L_{pc} > 2 \cdot \frac{E \cdot \mu G}{Z \cdot \beta \cdot 10^{15}\ eV} \tag{3}$$

with L_{pc} as the size of the accelerating region in parsec.
This equation allows the classification of objects with known sizes and magnetic fields

[1] One parsec (pc) is the distance under which the median distance from the Earth to the sun (One astronomical unit (AU)) is visible with an angle of 1 arc second. 1 pc = 3.16 ly

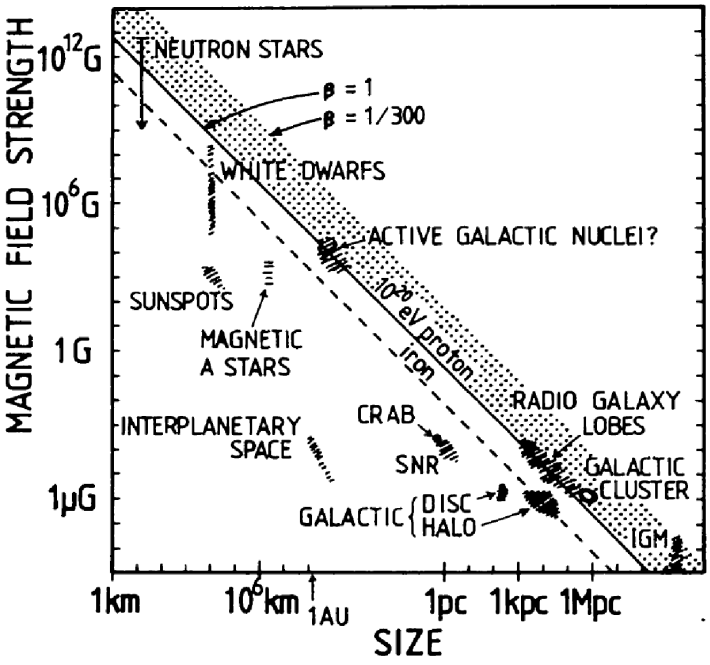

Figure 1: Hillas Plot showing size and magnetic field strength of possible sites of particle acceleration. Objects below the diagonal line cannot accelerate protons to $10^{20}eV$[10].

according to the maximal energy that can be produced. Such a classification is shown in figure 1, where the magnetic field strength of possible accelerators is shown against their size, ranging from kilometers up to mega parsecs. Lines of constant energy are diagonals from upper left to lower right. Objects to the left of such a line cannot accelerate particles to such energies. We see that not many objects remain that are candidates for the acceleration of particles to $3 \cdot 10^{20}$ eV, the highest energy detected. Only neutron stars, active galactic nuclei, radio galaxy lobes, galaxy clusters and intergalactic matter fulfill this relation. These object classes are the target of extensive studies because a direct identification of cosmic ray sources has not been achieved yet. A recent publication from the Auger collaboration [11] sees a correlation between the arrival direction of the highest energy cosmic rays and the position of active galactic nuclei.

3. The Propagation of Cosmic Ray Particles

After their acceleration, the cosmic ray particles travel through the universe. They are charged, therefore they interact with the magnetic fields of galaxies or the magnetic field between galaxies and become deflected by the Lorentz force. This effect is very strong for low energy particles, so that they are moving on chaotic trajectories and their arrival directions on Earth are completely randomized. The cosmic ray flux appears isotropic for low energies. The higher the particle energy, the smaller is the effect of magnetic deflection, and for particles with an energy higher than some 10^{19} eV this effect should

be so small that an identification of point sources should be possible for distances up to several decades of megaparsec [11].

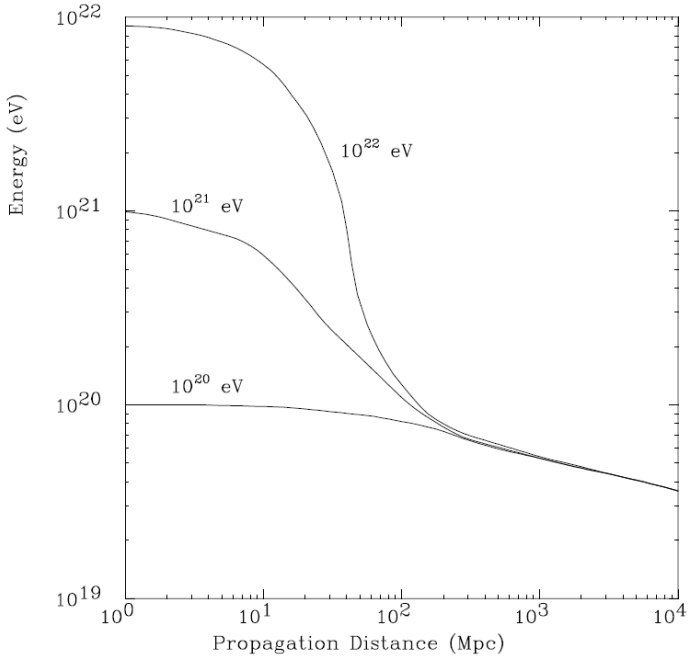

Figure 2: Energy loss for UHECR due to interaction with the cosmic microwave background for various starting energies [12].

One process influencing the cosmic ray particles is the Greisen-Zatsepin-Kuzmin effect (GZK-effect)[13][14]. The universe is filled with remnant photons from the big-bang. These photons form the cosmic microwave background (CMB) with a temperature of about 2.7 K. In the rest frame of a high energy cosmic ray proton with an energy over $\sim 5 \cdot 10^{19}\ eV$ these CMB-photons become high energy γ-photons and are able to interact with the protons, forming Δ^+ resonances. These Δ^+ resonances decay into protons, neutrons and mesons, with the baryons having a somewhat smaller energy than the incident protons. The main processes are:

$$\begin{aligned} \gamma_{CMB} + p \rightarrow &\Delta^+ \rightarrow p + \pi^0 \\ \gamma_{CMB} + p \rightarrow &\Delta^+ \rightarrow n + \pi^+ \end{aligned} \tag{4}$$

That means that protons with energies above the threshold loose a part of that energy consecutively until this particle reaction is energetically not possible anymore. Shown in figure 2 is the energy of ultra high energy cosmic ray protons over their propagation distance. We see that for a propagation distance greater than some 10^3 Mpc all cosmic ray particles have an energy of $\sim 5 \cdot 10^{19}\ eV$ regardless of the starting energy. That means that the visible cosmic ray energy spectrum has a natural upper boundary. This feature is called the GZK-cutoff.

4. The Energy Spectrum of Cosmic Rays

The energy spectrum is the flux of cosmic ray particles per energy interval of these particles. The energy spectrum is measured over several decades of energy and is shown in figure 3. It extends from 10^8 eV up to 10^{20} eV and beyond. Several experiments have reported cosmic rays with energies above 10^{20} eV, with $2 \cdot 10^{20}$ eV by the AGASA experiment[16] and $3 \cdot 10^{20}$ eV by the Fly's Eye experiment[17]. The highest energy measured by the Auger experiment is $2.2 \cdot 10^{20}$ eV [18]. We see that the spectrum follows a power law with an index of nearly 3, resulting in counting rates from 1000 particles per m^2 and second for the lowest energies and one particle per km^2 and century for the highest energies. A consequence of the steep spectrum is that only the lower parts of the spectrum are directly measurable, either by satellites or high altitude balloons. But common particle detector dimensions of several square meters are too small to detect the particles with higher energies in the time scale for such an experiment. The solution to this problem is the indirect detection of cosmic rays by instrumentation of large areas or the observation of large atmospheric volumes to measure extensive air showers (see section 5).
For energies above 10 GeV the energy spectrum can be parametrized by a power law:

$$\frac{d^2\Phi(E)}{dEd\Omega} \propto \left(\frac{E}{GeV}\right)^{-\gamma} \quad \frac{particles}{cm^2\ sr\ GeV} \tag{5}$$

The power index γ describes the steepness of the spectrum. In order to see deviations from the simple power law, a new representation where the energy scale is multiplied with a factor E^3 is used like in figure 4.
In this representation the form of the spectrum resembles a human leg, and therefore the visible features are called "knee", "ankle" etc. The knee is the region around 10^{15} eV, at this point the steepness of the spectrum changes from 2.7 for energies lower than 10^{15} eV to 3.1 for higher energies. In the ankle region with 10^{18} eV the steepness becomes flatter again with $\gamma = 2.7$. General explanations for these and other features are the transition from one acceleration source class to an other, the change of source locations or a change in the composition of particles. The feature of the knee is explained by a change in the composition if the cosmic ray particles [19][20]. The feature of the ankle is explained as change in the sources of cosmic rays: The magnetic field in our galaxy is of the order of 0.3 μG. A cosmic ray particle with an energy of 10^{18} eV in this field has a gyroradius of about 10^5 pc (see equation 1), that is the dimension of the galactic halo. Cosmic ray particles with such an energy can not be contained inside the galaxy. It follows that particles with an energy greater than 10^{18} eV are not of galactic but of extragalactic origin. The ankle marks the change from galactic to extragalactic sources. Cosmic Rays with an energy higher than 10^{18} eV are called Ultra High Energy Cosmic Rays (UEHCR's).

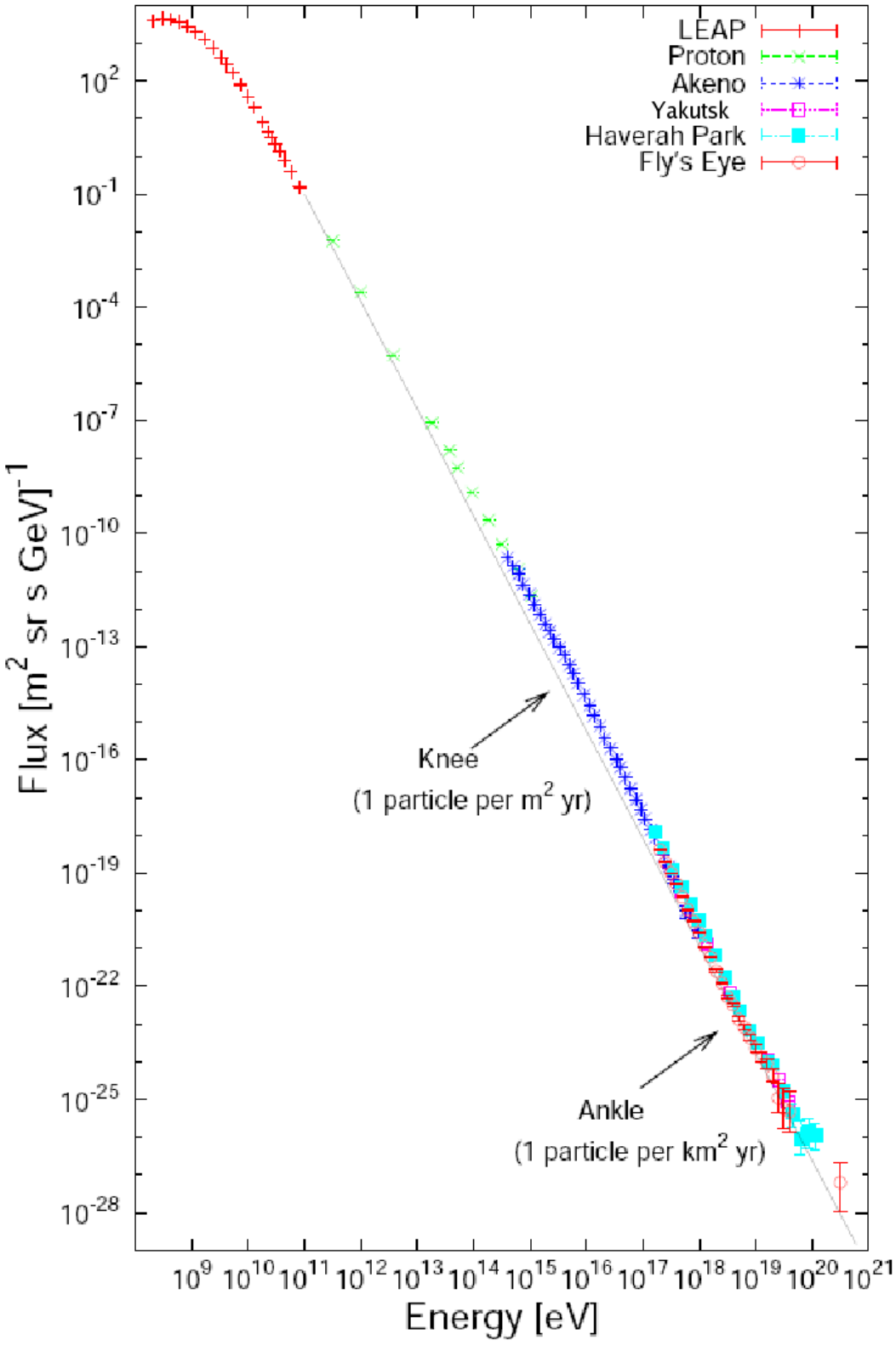

Figure 3: Flux of cosmic ray particles over energy per particle. To better show deviations from a power law the black line with constant steepness of 2.7 was drawn.(from [15])

Recent results from the Pierre Auger Observatory show that the cosmic ray spectrum does not continue over $10^{19.6}$ eV as a power law spectrum [21]. The observed flux suppression is interpreted as a sign of the GZK-cutoff. In figure 4 the upper end of the energy spectrum measured by the Pierre Auger Observatory is shown. The flux was multiplied with E^3 to make changes in the steepness of the flux better visible.

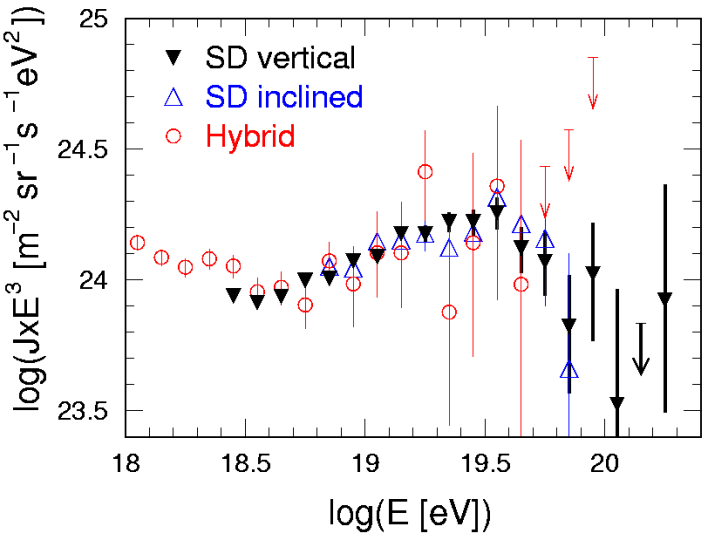

Figure 4: Flux of cosmic ray particles multiplied with E^3 over energy per particle measured at the Pierre Auger Observatory. (From[21])

5. Extensive Air Showers

The Earth's atmosphere consists of 78% nitrogen, 21% oxygen and 1% minor components, mostly noble gases. It extends from the surface up to several hundred kilometers with exponential decreasing density, so that an upper boundary of the atmosphere does not exist. At the highest altitudes of several hundred kilometers it consists of single non interacting molecules and not of a gaseous medium anymore.
The atmosphere is described by the integrated column density or atmospheric depth X in g/cm^2. The whole atmosphere has a column density of about $X_{atm} = 1000\ g/cm^2$.
The propagation of particles through matter is described by the interaction length λ for hadrons and the radiation length X_0 for electrons/positrons and photons. For air the radiation length has a value of $X_0 = 37\ g/cm^2$ and the interaction length a value of $\lambda = 90\ g/cm^2$ [22]. It is possible to describe the Earth's atmosphere as a particle calorimeter with $\sim$ 27 electromagnetic radiation lengths and $\sim$ 11 hadronic interaction lengths.

A cosmic ray particle that enters the Earth's atmosphere will have its first interaction at an altitude of 15 km to 20 km. If the primary particle is not a proton but a heavier nucleus with mass number A and energy E, the interaction can be described as an

interaction of A protons with energy E/A. The first interaction starts a hadronic cascade, consisting mainly of pions (π^0,$\pi^{\pm}$,90%) and kaons (K^0,$K^{\pm}$,10%). The charged pions and Kaons interact with air nuclei, producing again pions and kaons and form a hadronic cascade. Not reacting kaons decay after a short time into a muon and a neutrino or into two to three pions. Charged pions decay into muons and muon-neutrinos. Neutral pions decay into 2 photons that produce electrons and positrons by pair-production. That is the start of the electromagnetic part of the cascade. The whole cascade of secondary particles is called an extensive air shower (EAS).

Every step of this cascade distributes the initial energy of the primary cosmic ray particle to many secondary particles, until the energy per secondary particle is too low to allow further reactions. These "low" energy particles still loose energy by ionisation of the surrounding air and travel on until they reach the ground or are absorbed in the atmosphere. Particles that reach the ground can be measured with particle detectors.

The particles of the shower excite nitrogen molecules in the air. These excited molecules begin to radiate fluorescence photons with wavelengths in the visible and ultraviolet part of the electromagnetic spectrum. These photons can be observed with optical detectors, so called fluorescence telescopes.

The number of secondary particles, and therefore the size of the cascade depends on the energy of the primary particle. A primary particle of energy $10^{19}\ eV$ produces about $7 \cdot 10^9$ charged particles at shower maximum [23].

The longitudinal and lateral profiles of air showers can be parametrized by two equations, that depend on the altitude of the first interaction X_p. This point varies from shower to shower in the order of the interaction length X_0. Weather and other processes in the atmosphere can change its density and structure. These changes introduce fluctuations in the shower development.

The longitudinal shower profile can be described by the Gaisser-Hillas formula [24]. It parametrizes the number of charged particles $N(X)$ in the shower for a given atmospheric depth X:

$$N(X) = N_{max} \cdot \left(\frac{X - X_p}{X_{max} - X_p} \right)^{\frac{X_{max} - X_p}{\lambda}} \cdot e^{\frac{X_{max} - X}{\lambda}} \tag{6}$$

N_{max} is the maximum number of charged particles, X_{max} is the atmospheric depth where this maximum occurs, X_p is the atmospheric depth of the first interaction and λ is a fit parameter describing the shower shape. For the position of the shower maximum X_{max} exists an approximation:

$$X_{max} \simeq (1 - B) X_0 \left(\log \frac{E_p}{\epsilon} - \log A \right) \frac{g}{cm^2} \tag{7}$$

E_p is the energy of the primary cosmic ray particle, A is the mass of the particle and ϵ is the critical energy in air (81 MeV)). B describes the type of the cascade, B=0 for fully electromagnetic and B=1 for fully hadronic cascades. For an iron nuclei as heaviest particle X_{max} is about 100 g/cm^2 smaller than for a proton as lightest primary particle. This difference allows the identification of the primary particle if the longitudinal shower profile is measured because the shower maxima for heavier particles occur higher in the

atmosphere.
For ultra high energy cosmic rays the depth of the shower maximum lies between 700 g/cm^2 and 800 g/cm^2 for vertical showers. These showers reach the ground at 1000 g/cm^2 shortly after their maximum. For inclined showers these values are changed. The individual secondary particles have slightly different energies and slightly different lateral momenta, so they reach the ground with a time difference that is higher for heavier particles (hadrons) than for the lighter muons. In addition this time difference becomes greater with increasing distance to the shower axis because of geometric reasons.

The lateral shower profile is described by the Nishimura-Kamata-Greisen formula [25][26][27]. The secondary particles have a transverse momentum with respect to the shower axis. This leads to a spread in shower radius for the later parts of the shower development. An approximation for this behavior, that was developed to describe purely electromagnetic showers, but is used to describe also EAS, is the NKG formula:

$$\rho(r) \propto \left(\frac{r}{r_M}\right)^{s-2} \left(1 + \frac{r}{r_M}\right)^{s-4.5} \tag{8}$$

Here $\rho(r)$ is the charged particle density in distance r to the shower axis and r_M is the Molière radius, which describes electromagnetic interactions in matter. In air it can be parametrized as:

$$r_M(h) = \frac{9,6}{\rho_{air}(h)}\ g/cm^2 \tag{9}$$

ρ_{air} is the air density in an altitude h. The parameter s is the shower age, calculated as:

$$s = \frac{3 \cdot X}{X + 2 \cdot X_{max}} \tag{10}$$

The effect of the geomagnetic field on the charged particles for the shower shape is negligible for showers with zenith angles $< 60°$.

6. The Pierre Auger Observatory

The southern site of the Pierre Auger Observatory is located in Malargue, Argentina. As of now 95% of the surface detector and the the whole fluorescence detector is completed. An additional northern site in Colorado, USA is proposed. The observatory is split in two sites to gain an exposure of the whole sky by measuring on the northern and southern hemisphere independently. The observatory is designed to measure cosmic rays with an energy above $10^{18}\ eV$. The southern site alone is the greatest EAS detector build so far and is stably taking data since 2004, albeit being still under construction. The detection of extensive air showers at the Pierre Auger Observatory is done with two different detection concepts which is called "hybrid approach".

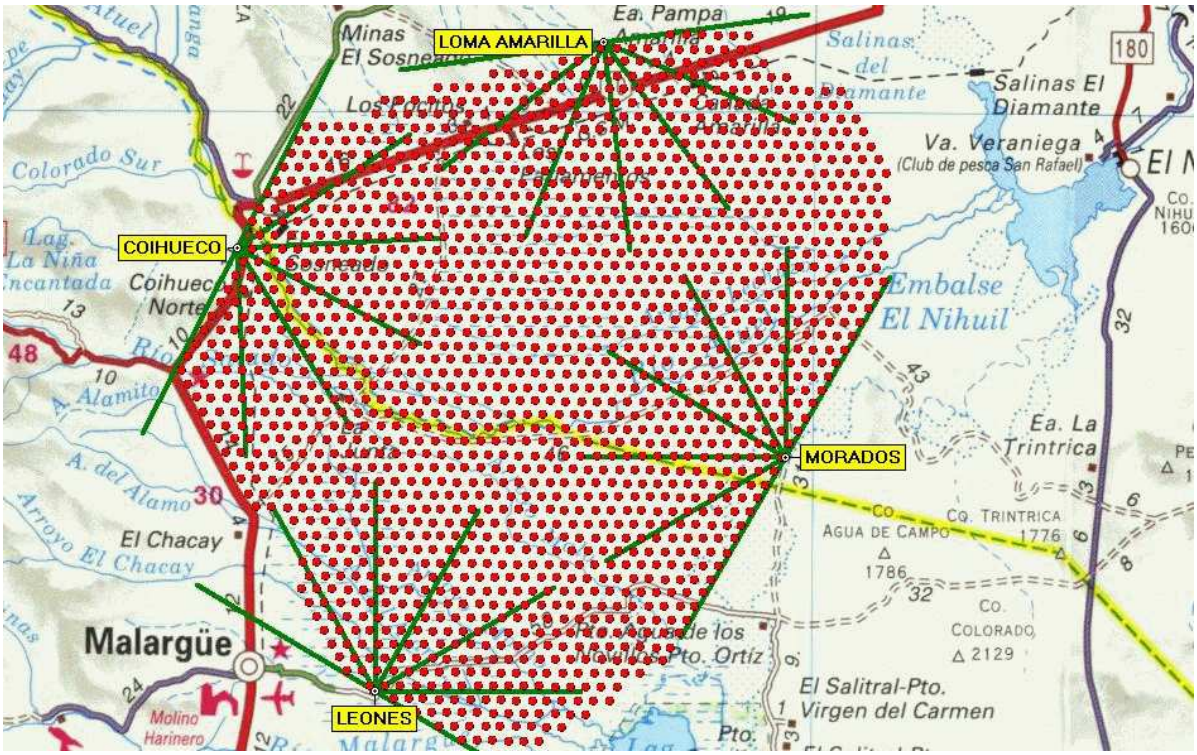

Figure 5: Layout of the southern site of the Pierre Auger Observatory located in Argentina. Each of the red dots represents one of 1600 surface detector stations. In the yellow boxes the names of the four fluorescence detector buildings are shown. The field of view for each telescope is shown with green lines.

6.1. The Surface Detector - SD

One observation method used at the Pierre Auger Observatory is the measurement of secondary shower particles at ground level with water Cerenkov detectors. That is done by covering an area of roughly 50 km times 60 km with a hexagonal grid of 1600 detector stations with a distance of 1.5 km between them. The instrumented area of 3000 km^2 is comparable in size to the German Bundesland "Saarland" (2568 km^2) or the US state "Rhode Island" (4002 km^2).
Each detector station is an independent water Cerenkov particle detector, consisting of a tank filled with 12 tons of ultra pure water that is watched by three photomultiplier tubes (PMT's). Each tank has its own data acquisition and local solar power supply. The measured data is transfered to a central station by mobile phone technology. The tanks are designed for minimal maintenance in the projected 20 year lifespan of the observatory.

The detection of particles in the tanks uses the Cerenkov effect: Electrons and muons from the shower that enter the tank are highly relativistic. They travel with a velocity close to the speed of light in vacuum and greater than the speed of light in the water and produce Cerenkov photons. These photons are reflected on the diffuse inner surface of the water tank and then registered in the PMT's where the photon signal is converted into an electric signal. The tank electronic generates a first level trigger when two PMT's register a coincident signal in a certain time window or one PMT registers a signal greater than a threshold. If the neighboring tanks have also registered a signal, the data from all the tanks is read out and designated as air shower candidate. From the time difference of the typically hit 3 to 10 tanks the shower axis is reconstructed. The lateral density function, reconstructed from the sampled density by the tanks, is used to calculate the energy of the cosmic ray primary.

Because the shower is sampled only at ground level Monte Carlo simulations have to be used to calculate the shower profile and gain information on the primary particle. It follows that values derived by this detection method have relatively high systematic uncertainties because the energy has to be reconstructed from Monte Carlo simulations. The SD array is designed for an energy resolution better than 12% and an angular resolution better than 1.1° for all events with an energy greater than $10^{19}eV$ [28]. Today this resolution is achieved for all events with an energy over $3 \cdot 10^{18}eV$ [29]. The SD has a high duty cicle of nearly 100% and is so capable of measuring a high number of extensive air showers.

6.2. The Fluorescence Detector - FD

The fluorescence detector measures photons generated by excited nitrogen molecules. The FD consist of four separate stations that are called "Eyes". The four Eyes are located on the border of the surface array at four different locations, so that the volume over the whole surface array is monitored. Each Eye has a field of view of 180° in azimuth and 30° in zenith. One Eye consists of six fluorescence telescopes with a field of view of

$30^\circ \cdot 30^\circ$. The telescopes are Schmidt-Telescopes and consist of a mirror and a camera. The camera consists of an array of 440 PMT's. Fluorescence photons generated by the air showers are projected by the optics system on the segmented mirror that focuses the photons on the PMT's. The time and intensity information for each PMT is processed.

The amount of fluorescence photons generated by the passage of high energetic particles, the so called fluorescence light yield, is known from dedicated experiments [30]. With this information a calorimetric measurement of the longitudinal shower profile and the position of the shower maximum is possible. The fluorescence detector is designed for an energy resolution of 5% [28]. As of today the resolution is calculated to be of the order of 10% [31]. A constraint on the operation of the fluorescence detector is the sensitivity of the PMT's, allowing measurements only in dark moonless nights, resulting in a duty cycle of only 10%.

6.3. Hybrid Detection

The so called "Hybrid events" are cosmic ray candidates that were seen in the fluorescence and surface components of the detector. The number of registered events is here again limited by the duty cycle of the fluorescence detectors, but these events allow an alternative energy calibration for events that were only detected with the SD component. The hybrid detection concept allows for a combination of the high angular resolution and high duty cycle of the surface detector with the high energy resolution of the fluorescence detector.

6.4. Radio Detection

One new detection method is currently studied at the Auger Observatory. The charged particles of the shower are travelling with a high velocity through the Earth's magnetic field and are deflected by the Lorentz force. Accelerated charged particles emit synchrotron radiation. This effect is called geo synchrotron radiation. The coherent emission of synchrotron radiation leads to radio pulses that are detectable by an array of radio antennas on the ground [1].

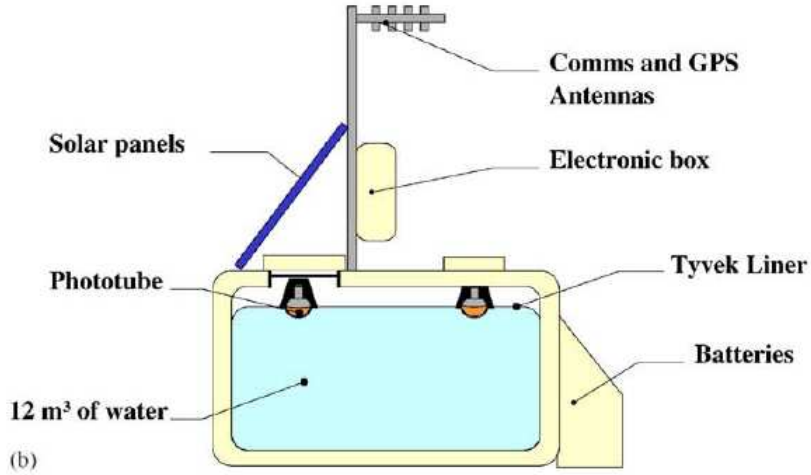

Figure 6: A schematic view of a surface detector station[32]. The Tyvek liner is an uniform reflecting plastic coating that reduces the absorption of Cerenkov photons by the tank walls.

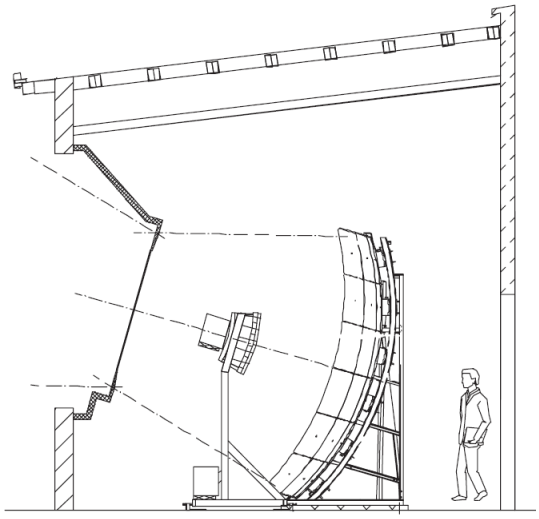

Figure 7: A schematic view of a fluorescence detector telescope[32].

Part III.
RADAR Detection

RADAR is short for Radio Detecting and Ranging. RADAR can be used to monitor huge volumes of atmosphere. The principle setup consists of the transmission of radio waves with a given frequency, power and modulation into the monitored atmosphere volume and than receiving radio waves scattered or reflected by objects in the volume or the atmosphere itself. From the power, the frequency and the modulation of the reflected waves one can then gain knowledge on several properties of the objects in the volume, such as distance, (radial) velocity and size of the object.

7. RADAR Geometries

There are two different geometries for a RADAR setup[33]:

When the transmitter and the receiver are closer than the used radio wavelength the setup is called "monostatic". When the distance between transmitter and receiver is greater than the radio wavelength the setup is called "bistatic". For some setups this distance can be several hundred kilometers. A network from several bistatic setups is called "multistatic". In it a single transmitter/receiver unit is able to receive scattered signals generated by itself and those generated by all other transmitters.

Another classification is the difference between forward scatter and back scatter geometries. In the forward scatter case the angle between transmitter - object line of sight and object - receiver line of sight is greater than 90° and in the back scatter case this angle is smaller than 90°. That means that all monostatic setups operate in back scatter mode.

Because the operation of RADAR transmitters is strictly regulated and costly one can use existing transmitters for a bistatic setup. By listening to scattered signals originating from an existing transmitter that is operated for a completely different purpose one can use a so called passive or parasitic RADAR setup. Usable types of transmitters are radio transmitters, television transmitters, ham radio beacons or even existing RADAR transmitters. The limitation in such a setup is the missing control or information about frequencies, emission characteristics and status of the transmitter.

8. RADAR Physics

A transmitter produces radio waves with a given frequency. Far from the transmitter, these waves can be described as plain waves. If these waves hit an object, they force the free charge carriers, mainly free electrons and sometimes ions in this object into vibrations with a frequency equal to that of the radio waves. Because accelerated charges emit radio waves, every electron radiates radio waves with the incident frequency like a Hertzian dipole. The combination of many radiating electrons leads to an isotropic

radiation. The isotropic radiation is modulated by the form of the surface where the electrons are located. For example the waves from different points of the surface can interfere, modulating the radiation profile. The scattered intensity is dependent on the actual scatter geometry. The detection of a part of this scattered radio waves allows then to gain information on the size of the scattering object. If only a short radio pulse is generated by the transmitter, the time difference between transmission and reception gives the range from the transmitter to the object. This basic principle of RADAR detection is easily expandable to give additional informations on the object and the scattering geometry (as shown in [34][35]).

8.1. The RADAR Equation

The received power P_R is given by the "RADAR Equation", shown here in a general version for the bistatic setup [35]:

$$P_R = \frac{P_T \cdot G_T \cdot \sigma \cdot A_R}{(4\pi)^2 \cdot {R_T}^2 \cdot {R_R}^2} \tag{11}$$

Where R_T is the distance from the transmitter to the scattering object, R_R is the distance from the object to the receiver. P_T is the transmitter power, G_T is the gain of the transmitting antenna[2], σ is the radar cross section (rcs) of the scattering object meaning the effective scattering surface and A_R is the effective surface of the receiving antenna, called aperture. The received power becomes smaller with R^4 which makes it necessary to have a setup that is capable to detect very weak signals.

If the range between transmitter and scattering object is measured as described above this equation allows the calculation of the rcs of the scattering object and so information on the geometry of the object.

For a monostatic setup the equation is simplified:

$$P_R = \frac{P_T \cdot G_T \cdot \sigma \cdot A_R}{(4\pi)^2 \cdot R^4} \tag{12}$$

R is the range from transmitter to the scattering object.

8.2. Doppler Effect

To describe the frequency shift originating in the Doppler shift of a moving object it is helpful to define the bistatic range sum $R_b = R_T + R_R$. It is simply the sum of the distances between transmitter and object and between object and receiver. A definition of the bistatic Doppler shift $\Delta\nu_b$ without relativistic effects (all velocities small compared to the speed of light) is given as time rate of change of the bistatic range sum, normalized by the wavelength λ [33].

$$\Delta\nu_b = \frac{1}{\lambda}\left(\frac{d}{dt}(R_T + R_R)\right) = \frac{1}{\lambda}\left(\frac{dR_T}{dt} + \frac{dR_R}{dt}\right)\ [Hz] \tag{13}$$

[2] A characteristic that describes the directivity of an antenna compared to isotropic radiation, see appendix.

In the standard bistatic case with a stationary transmitter and receiver and a moving scattering object this can be simplified: The projection of the object velocity on the transmitter - object line of sight is V_T, the projection on the object - receiver line of sight is V_R. Then we get:

$$\frac{dR_T}{dt} = V_T \ [m/s] \tag{14}$$

and

$$\frac{dR_R}{dt} = V_R \ [m/s] \tag{15}$$

Combining these formulas gives:

$$\Delta\nu_b = \frac{V_T + V_R}{\lambda} \ [Hz] \tag{16}$$

In the monostatic case, with $R_T = R_R$ and $V_T = V_R = V$ and V the radial velocity towards the transmitter / receiver unit we get:

$$\Delta\nu_b = \frac{2 \cdot V}{\lambda} \ [Hz] \tag{17}$$

That means motions that reduce the (bistatic) range sum lead to higher frequencies than the original transmitter frequency. Motions that enlarge the distance lead to lower frequencies.

9. Phenomena detectable by RADAR

Objects detectable by RADAR are objects that can reflect or scatter radio waves. There are two classes of these objects, either massive bodies or regions of high ionisation.

The detection of massive objects by RADAR was first patented by Christian Hülsmeyer in 1904 [35]. Today this principle is used in a wide range of applications, for example:

Air traffic control The measurement of airplane positions and velocities, both civilian and military use

See traffic control The measurement of ship positions and velocities, both civilian and military use

Speed measurements Traffic control on streets or in production cycles

Astronomic use Measurements of distances and rotation periods of planets in our solar system

RADAR measurements are established but the field is today still the target of research.

Somewhat younger than the detection of massive bodies is the detection of regions of high ionisation. Here the scattering is done by free electrons and ions in a medium, not bound charge carriers in a massive body. This technique is used in a wide range of scientific research, for example:

Atmospheric Studies Several regions of high ionisation exist in the Earth's atmosphere. These regions are influenced by the solar wind and the interplanetary magnetic field.

Lightning Strikes Lightning strikes produce a short lived region of high ionisation that is detectable by RADAR.

Meteor Science When meteors enter the Earth's atmosphere they produce a trail of high ionisation that is measured to gain information on some parameters of the originating meteor.

In addition any process that produces regions of high ionisation should be detectable by RADAR.

Part IV.
Meteor Science

Meteors are one class of objects that is able to produce regions of high ionisation that are detectable by RADAR. A recent theoretical analysis from Peter Gorham[36] comes to the conclusion that the ionised regions generated by meteors and those generated by EAS should be similar in many aspects. Meteors can be used to study the scattering of radio waves at ionisation clouds similar to those of EAS.
To understand the processes that form these ionised regions, a short introduction on the physics of meteors is given. These results were gained in nearly 100 years of meteor research[3], experimentally and theoretically, done by a large number of scientists and were presented in a review on meteor science by Ceplecha et al. [37]. The following part is based on that review and only results are presented.

10. Meteor Physics

The solar system is filled with particles composed of dust or rock. The size of these particles is limited on the lower side by their detectability with different methods to around 0.01 mm and on the upper side to several tens of meters[4]. The international Astronomic Union defines this class of objects as meteoroids. If such an object comes into contact with the Earth's atmosphere and interacts with it, it is called a meteor. Should some part of the object survive the interaction with the atmosphere and reach the ground it is called a meteorite. In figure 8 the size of meteors is compared with other known objects of the universe. The class of meteoroids is divided into the several detection methods with which these objects can be detected. Fireballs are meteors that can be observed with the naked eye. Photographic meteors are found by looking at long exposure pictures of the night sky. TV meteors are detected by filming the night sky with video cameras. Radar meteors are detected by the measurement of scattered radio waves. The basic terminology of meteors is shown in figure 9.

The origin of meteoroid objects is linked to several sources: A part of the meteoroids are leftover from the formation of large bodies in the solar system. Another part are the product of the total disintegration of a large cometary body. These are non regular comets occasionally entering the inner solar system from the Oort cloud. Some are fragments of asteroids that where shot off at an impact of a small body onto an asteroid. The last part of the meteoroid population are objects left behind on their trail by the slowly disintegration of regular comets, so called shower meteors (see section 10.1).

[3]The first study of meteors that was done with other means than the human eye was performed by L. Weinek in 1885 by photographing meteors.

[4]The next larger class of objects is typically called asteroids with a size larger than 100 meters. The boundary of these two object classes is not well defined.

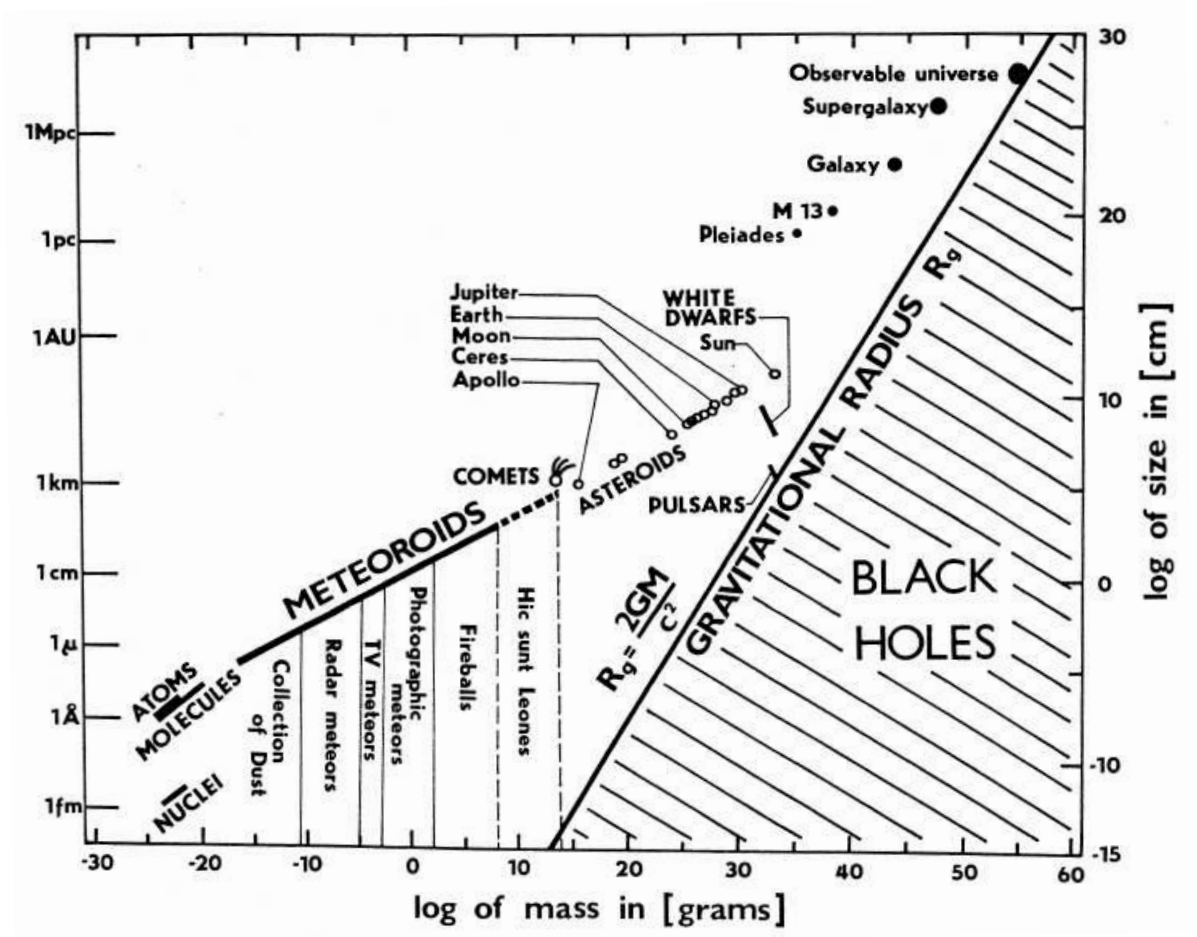

Figure 8: Diagram of size versus mass of some known objects of the observable universe [37].

Most of our knowledge about meteoroids comes from the very short time of their atmospheric interaction. Any knowledge gained from measuring meteor phenomena is therefore biased by the condition that the orbit of the Earth and the orbit of the meteoroid have to intersect.
The atmospheric entry of a meteor is a collision of two astronomic objects. For meteoroids bound in the solar system the velocities at the contact point with the Earth's atmosphere are limited. These limits can be derived from the Kepler kinematics of objects bound in the gravitational field of the sun.
The lower velocity limit is the speed of an object that moves incidentally with the same speed and on the same trajectory as the Earth. In a coordinate system with origin at the center of the Earth such a particle is at rest. Assuming that the particle is accelerated only by Earth's gravity it reaches a velocity of 11.2 km/s when it collides with the Earth.
The upper velocity limit is the sum of two velocities: The first is the highest velocity the Earth can achieve on its trail when it is closest to the sun (the perihelion): 30.3 km/s.

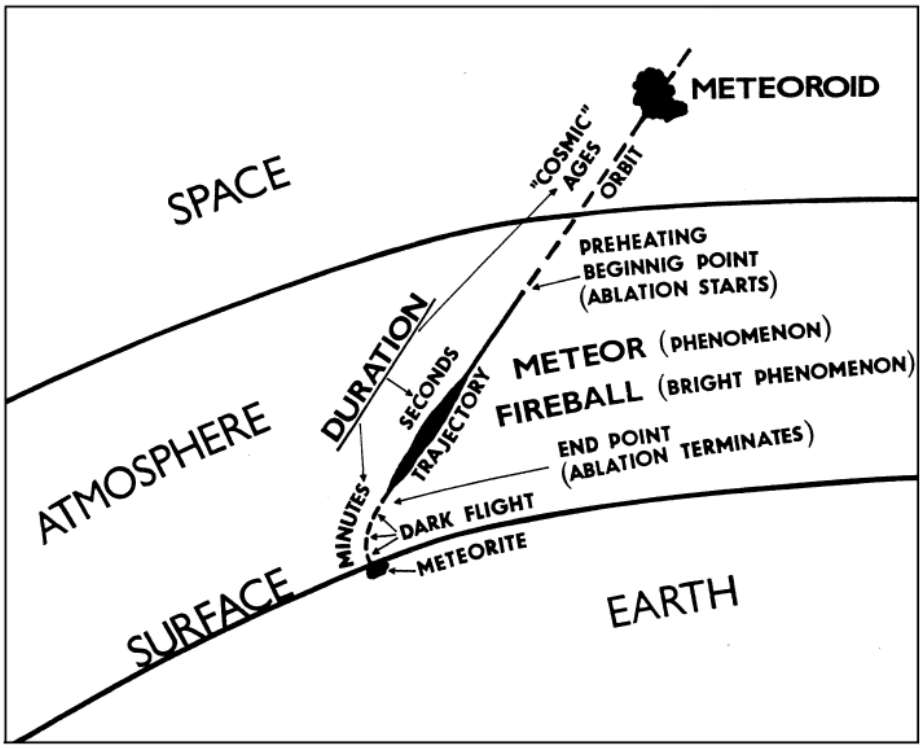

Figure 9: Basic terminology of meteors[37].

The second part is the velocity of an object on a parabolic trajectory at the distance to the sun of the Earth's perihelion(all bound objects have a smaller velocity). This velocity is 42.5 km/s, giving the upper limit of 72.8 km/s. Objects not bound in the solar system can create higher collision speeds, however studies with several detection methods found an upper limit of 2% of all sporadic meteors with higher velocities than bound objects.

The interaction of meteors with the Earth's atmosphere produces several secondary effects that are observable with different techniques:
Some meteors produce light in the visible spectrum range. This light can be detected with photographic or video observations of the sky or the human eye. In addition this light can be studied by a spectral analysis to gain information on the chemical elements producing the light emission. Sounds generated by meteors, often infrasound with very low frequencies but sometimes sounds audible by the human ear, can be measured with acoustic setups or seismic observatories.
Regions of high ionisation are generated by nearly all meteors. Dependent on the size and ionisation density of a certain region these can scatter radio waves, allowing a detection with RADAR.
Not all detection methods are possible for all types of meteors, because of different size, composition and velocity of the original meteoroid.

The number of interplanetary bodies that collide with the Earth per year depends on

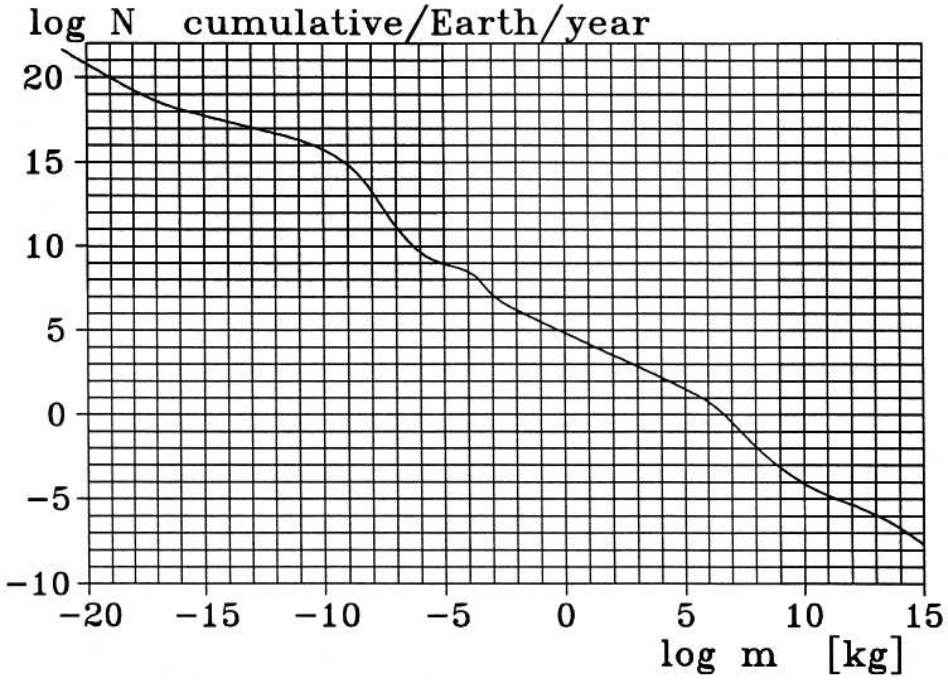

Figure 10: Cumulative number N of interplanetary bodies with mass equal or greater than m reaching the Earth's surface per year against the mass m[37].

the mass of these bodies. The number of small bodies is many orders larger than that of larger bodies. This dependence is shown in figure 10.

10.1. Meteor Classes

Meteors are roughly categorised into two classes:

Meteor showers are associated with comets. Regular reoccurring comets exist with periods from one up to several hundred years. On their journey around the sun they loose dust and other small particles. These particles continue to circle the sun on slightly different trajectories than the comet, so that after several periods around the sun the space along the comets trajectory is filled with a cloud of particles, so called meteoroid streams. For some comets these trajectories cross the Earth's path, leading to an abrupt rise in meteor counts on the same days in each year when the Earth is moving through such a particle cloud. These meteors are called meteor showers or meteor streams. Because the celestial mechanics for the crossing of the Earths and comets trajectories are known the exact time of such a meteor shower is known way before the shower actually happens. This allows the measuring of a high count of meteors on a given date in contrast to the hope of seeing a sporadic meteor by chance. Visual counting rates for meteor showers can reach several hundred meteors per hour.[5]

Sporadic meteors are meteors not associated with meteor showers. Their counting rate (on a fixed position on Earth) is modulated with a diurnal and a seasonal period. The seasonal period is explained by a different density of meteoroids in different parts of the solar system that the Earth crosses at different times in the year.

The diurnal variation, highest counting rate at the local time of sunrise and lowest counting rate at the local time of sunset can be explained by the geometry of the Earths motion: At the local time of sunrise looking directly up is looking into the direction the Earth is moving on its trail around the sun. Looking directly upwards at the local time of sunset is looking against the direction of the Earth's movement around the sun. The velocity distribution of meteoroid particles has a maximum velocity of 42.5 km/s. That is higher than the maximum orbital velocity of the Earth of 30.3 km/s. It follows that at the time of sunrise the atmosphere can catch all meteoroids that are moving against the Earth and the particles that are moving into the same direction as the Earth up to a velocity of the Earth's velocity. At sunset the opposite occurs, only the small fraction of meteoroids that move in the same direction as the Earth and are faster than the Earth with 30.3 km/s can reach it from behind. This process is analogous to the difference in the apparent rainfall rate when observed through the windscreen and rear window of a moving vehicle [38]. The counting rates at dawn were found to be four times higher than those at sunset. Compared with meteor showers the sporadic meteors have greater absolute counting rates, nearly 75% of all visual meteors are sporadic meteors.

[5] So called meteor storms are short lived outbursts in meteor activity and are produced by the crossing of he Earths path trough a recently developed region of high particle density in a meteoroid stream (because the comet traveled this part of his track only a short time ago for example).Visual counting rates for such a meteor storm can reach 150 000 meteors per hour.

10.2. Ionisation Produced by Meteors

In the following the physics of ionisation by meteors is explained. For a detailed description of the other possible detection methods and their physics see the review of Ceplecha et al.[37].
A meteor that is traveling with a high velocity through the atmosphere is loosing atoms by evaporation. The major process responsible for the evaporation is heating of the surface of the meteor body. The inelastic collision of these vaporized atoms with air molecules ionises the air molecules and produces a trail of ionisation as the meteor moves on.

With β as the number of free electrons produced per meteor atom, μ the average mass of a meteor atom, V the velocity of the meteor and $\frac{dm}{dt}$ the loss of mass rate the number of electrons produced is given as:

$$q = -\frac{\beta}{\mu V}\frac{dm}{dt}\left[\frac{1}{m}\right] \tag{18}$$

β is in the order of 0.1 electrons produced per meteor atom. The mean atomic mass was found to be $\mu = 40$. Most of the meteors detectable by RADAR have a mass smaller than 10^{-5} kg, corresponding to a radius of around 0.1 cm. Studies of the loss of mass process showed that individual ionisation trails can extend over an altitude range of 10 km to 15 km. The ionisation density distribution along the trail can be described as a parabolic function of the atmospheric density at the altitude of maximum ionisation. Theoretical calculations of the loss of mass process found the maximum line density of the ionisation (the number of electrons per meter) to be proportional to the initial meteoroid mass and the cosine of the zenith angle of the ionisation trail.

The starting altitude of the ionisation trail was calculated to be around 120 km for fast meteors (70 km/s) and around 80 km for slow meteors (11 km/s). Theoretical values for the altitude of maximum ionisation for different meteor velocities are presented in figure 11 for two different maximum line density values. Similar to air showers the maximum density depends on the energy/mass of the meteor. Higher masses create more ionisation and maxima higher in the atmosphere. The higher the speed, the earlier the ionisation trail builds.

Theoretical calculations and measurements of the initial radius of the ionisation columns are inconsistent. In theoretical calculations it was found that the lateral profile of the ionisation is not a Gaussian distribution, but shows that a region of high ionisation with a sharp boundary is surrounded by a more diffuse area of lower ionisation density. The radius of the inner core is inversely proportional to the atmospheric density.
The inconsistencies between theory and measurements were partially solved by the introduction of an effective radius of the ionisation column, when a theoretical non Gaussian ionisation trail is assumed to scatter radio waves as if it had a Gaussian radial distribution. Values for the initial column radius r_0 found in measurements range from 0.2 meters up to 10 meters.
After the initial formation of the ionisation column the ionisation density begins to dissipate. The processes that reduce the ionisation density are ambipolar diffusion, at-

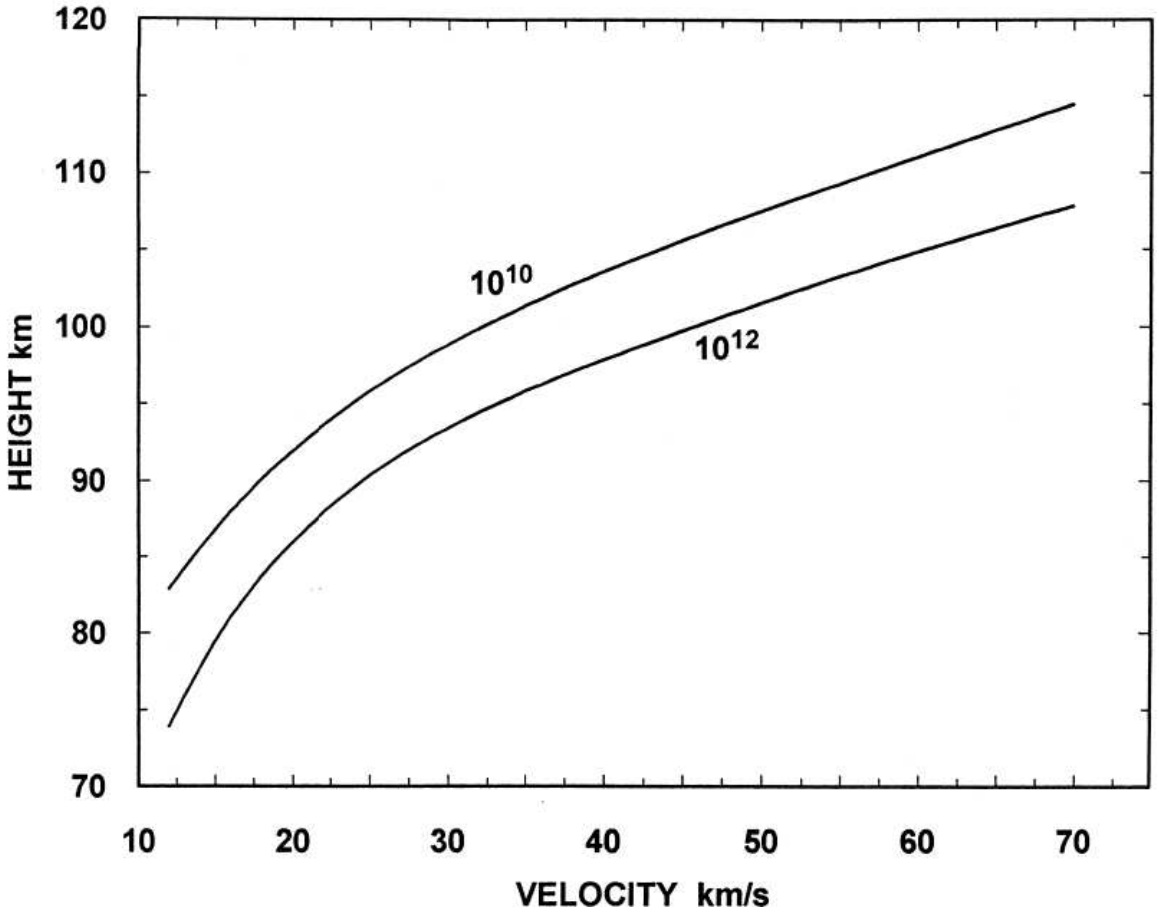

Figure 11: Altitude of point of maximum ionisation as function of velocity, shown for two values of maximum line density of ionisation, 10^{10} and 10^{12} electrons per meter.[37]

mospheric turbulence and loss of ionisation through recombination and ionic reactions. Ambipolar diffusion describes the diffusion of positive and negative charged particles in a plasma with the same rate due to their interaction via an electric field. In addition a bending and twisting of the whole trail can be caused by large scale wind shears.
The dominating effect in the dissipation process is ambipolar diffusion, which leads to a reduction in volume density but leaves the line density constant. Taking magnetic effects into account possible column shapes range from cylindric to elliptic cross sections.
The atmosphere in which the trail formation happened is not stationary. Typical horizontal velocities for the atmosphere in altitudes where the ionisation trails are formed are of the order of 100 m/s. Wind shear, that is the velocity differential between different points of the trail, has a typical size of 5 $\frac{m}{s}$ $\frac{1}{km}$. The ionisation process ends when the velocity of the remaining meteor body is too small to produce ionisation or the meteor body has completely disintegrated. For sporadic meteors this is normally the case at altitudes above 65 km.

10.2.1. Underdense and Overdense Trails

Ionisation trails can be classified as underdense or overdense:
The trail is called underdense when secondary scatter of radio waves between the electrons in the trail is very small. In this case radio waves can penetrate the column nearly unchanged and the total scattered radiation is the sum of the contributions from individual electrons. Ionisation columns with line densities smaller than 10^{13} electrons per meter satisfy this condition.
If the line density of the trail is higher than 10^{15} electrons per meter the trail is called overdense. In this case secondary scattering of radio waves between electrons has a large effect. The scattering of radio waves on overdense trails can be described by modeling the trail as a metallic cylinder. Overdense trails reflect radio waves at their surface. This cylinder expands with the diffusion of the trail until the line density changes into the underdense regime and the overdense trail vanishes and the trail becomes underdense. In addition every overdense trail is surrounded by an underdense region.
The transition value from underdense to overdense is a line density of 10^{14} electrons per meter, independently from the wavelength of the radio waves.

10.3. Ionisation Trails

The ionisation trails generated by meteors can be characterized by several properties:

- The trails are produced at an altitude of 70 km to 120 km.
- The whole trail is moving with the velocity of the atmospheric layer in which it was produced. If the trail lies in several atmospheric layers that move differently parts of the trail are separated. That is called wind shear.
- Depending on the angle between the movement direction of the meteor and the zenith the trails can reach lengths of up to several decades of kilometers.
- The initial cross section of the trail is of cylindric or elliptic shape.
- The initial radius of the trail ranges from 1 m to 20 m.
- The initial line density of ionisation is higher in the middle of the trail than on the starting and ending points.
- The limited velocity of the meteor leads to time differences for the initial ionisation production between early and late parts of the trail. This time difference can reach the order of several seconds for slow meteors.
- After the ionisation production diffusion processes lead to a growing radius of the trail with time. This leads to a declining ionisation density with time.
- Some time after the ionisation production the ionisation density of the trail reaches the ionisation density of the surrounding atmosphere.

10.4. Scattering of Radio Waves on Ionisation Trails

The scattering of radio waves on ionisation trails is very complex and depends on many parameters. It is possible to develop a compact equation for the received power P_R with several approximations [39]:
The trail is assumed to be of infinite length and of cylindrical shape. The electron distribution is assumed to be of Gaussian shape in radial direction. The electron density is low enough that individual electrons behave like Hertzian dipoles. For the received power P_T as a function of time follows:

$$P_R(t) = \frac{P_T G_T G_R \lambda^3 \sigma_e}{64 \cdot \pi^3} \cdot \frac{q^2 S}{R_T R_R (R_T + R_R)(1 - \sin^2\phi \, \cos^2\beta)} \cdot \exp\left(-32\pi^2 \frac{Dt \, \cos^2\phi}{\lambda^2}\right) \cdot \exp\left(-8\pi^2 \frac{{r_0}^2 \, \cos^2\phi}{\lambda^2}\right) \quad (19)$$

where P_T is the transmitter power, G_T and G_R are the transmitter and receiver gains, λ is the wavelength of the used radio waves, σ_e is the scattering cross section of a free electron, q is the electron density, D is the diffusion constant, S the polarization coupling factor, β is the angle of the trail relative to the plane formed by R_T and R_R, ϕ is the propagation angle, and r_0 is the initial trail radius.

This equation is a modified version of the RADAR equation in section 8.1. From it we can draw several conclusions for meteor scatter signals:

- The maximum intensity is proportional to λ^3
- The duration of meteor scatter signals is proportional to $1/\lambda^2$

It follows that meteor scatter signals are stronger and longer for higher wavelengths or lower frequencies. That means that for a given transmitter power and given receiver sensitivity setups with lower frequency can detect meteor scatter signals from weaker ionisation trails and these signals are longer than those for higher frequencies.

10.5. Comparison of Meteor and EAS generated Ionisation Columns

The ionisation trails generated by meteors and EAS are similar in many features.
RADAR detected meteors occur at an altitude of 80 km to 120 km. They produce ionisation columns with line densities of $\alpha = 10^{13}\ m^{-1}$ to $10^{16}\ m^{-1}$. The smallest detectable meteors have a mass of about 1 μg and a radius of around 100 μm. For typical meteor velocities the kinetic energy of such a meteor is 0.05 Joules. A large part of this energy goes into ionisation along the meteor's path.

Cosmic ray protons with an energy of 10^{18} eV have a kinetic energy in the order of 0.1 Joule. A large part of this energy goes into ionisation of the air around the developing air shower. The point of first interaction is located at an altitude of 20 km. The initial electron density of the ionisation columns of meteors and EAS is different because

the meteor trail is produced by a single body with an upper velocity limit of 80 km/s whereas the EAS ionisation column is generated by many secondary particles traveling nearly with the speed of light, resulting in an quasi instantaneous buildup of the EAS ionisation column.

After the initial buildup the density of both columns evolves because of atmospheric effects. Here a large difference between both type of columns develops, because the atmospheric properties for the two altitudes are different. The main difference comes from the different diffusion coefficients D, leading to different decay times for the two altitudes. The power of the RADAR echo decays with a time constant $\tau = \lambda^2/(32\pi^2 D)$. For meteor altitudes D is the ambipolar diffusion coefficient and has values between 1 $m^2 s^{-1}$ and 10 $m^2 s^{-1}$. This leads to decay times of several ms for frequencies between 10 MHz and 100 MHz. Because of the limited velocity of the meteor there is a time difference between the ionisation buildup for the starting point and the ending point of the trail. This leads to a difference in the time when radio wave scattering is possible for different parts of the trail. The total duration of an meteor scatter signal can reach 20 seconds or more when radio waves are scattered on several different points of the same trail over time.
For the ionisation produced by EAS additional diffusion processes at lower altitudes have to be taken into account. An upper limit for the free electron lifetime is found to be 20 ms and a lower limit of 20 μs [36]. The mean value of the lifetime lies towards the lower limit of this range. Theoretical calculations for the radar cross section lead to values which are comparable or higher than those of meteor generated ionisation columns, see [36]. The high velocity of the EAS leads to an instantaneous production of the ionisation trail. There is no time difference between the beginning of the diffusion process for early and late parts of the trail. The ability to scatter radio waves is the same for the whole trail resulting in much shorter scattered signals. It follows that EAS generated ionisation columns should be detectable with slightly modified meteor scatter setups. The main differences are the scattering geometry because of the much lower altitude and the much shorter signals, leading to higher requirements for the time resolution of the setup.

11. Meteor Scatter - The RADAR Principle as a Communication Channel using Meteors

One of the goals of radio communication is a large distance between transmitter and receiver. Standard setups are limited in their range by the curvature of the Earth, allowing communication only when transmitter and receiver are in their respective fields of view. To cover even longer distances several over-the-horizon communication channels have been developed, one of them is the technique called Meteor Scatter (MS). Here the signals from the transmitter are reflected on ionisation columns generated by sporadic meteors, allowing transmission of signals over distances of 800 km to 2000 km. This communication channel is used commercially in several applications. For example

meteor scatter communication is used for remote weather measurement stations of the US agricultural services, SNOTEL [6]. The use of meteor scatter channels as long range backup is used by several military organizations over the world. For an overview of existing meteor scatter applications see the book on meteor burst communication from J.Z. Schanker [40].

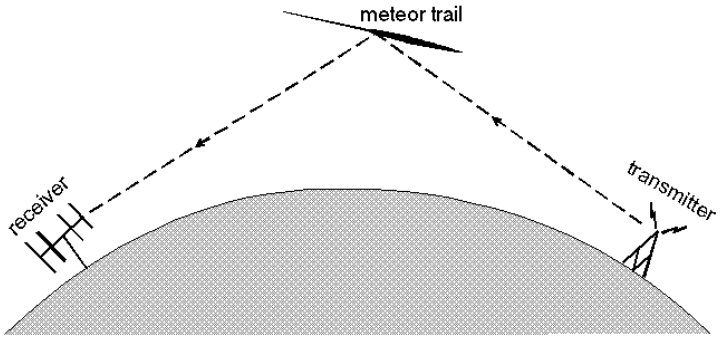

Figure 12: Meteor Scatter Schematic

Meteor scatter is also used by ham radio amateurs. Because this communication channel relies on sporadic meteors a direct two way communication is impossible. The transmission of information is usually achieved by the continuous repetition of the signal until it is acknowledged by the recipient. Because the lifetime of an ionisation column is too short to transmit the whole signal, advanced receiving software combines several received signal fragments scattered on several ionisation trails. One way to boost the message throughput is the use of prerecorded messages that are transmitted time compressed. So it is possible to transmit more information over the same ionisation trail. The maximum range for meteor scatter communication is over 2000 km for advanced setups and radio quiet times. A schematic overview of a meteor scatter transmission is shown in figure 12.
The ham radio community is very well organized around the world. To provide a method to check one's setup several ham radio amateurs operate radio beacons. That are unmanned transmitters that transmit with known values of power, frequency and direction. Some of these beacons transmit constant monofrequent signals whereas other transmit their call signs or use some kind of modulation. With the use of these beacons it is possible to test the receiving part of a radio equipment and the atmospheric conditions between beacon and receiver. Radio transmission is highly regulated. Because of that every person that is allowed to transmit on ham radio bands and every beacon has to be identified by an unique call sign. These call signs are 5 or 6 digits long. In the first two digits the nation where the transmitter usually is located is transcribed. Every user of an ham radio band has to identify himself by transmission of his call sign when initiating a communication attempt.

[6] See http://www.wcc.nrcs.usda.gov/snow/about.html for details

Meteor scatter is the topic of ongoing research. Theoretical calculations and measurements are regularly presented in scientific journals, for example [41] [42] [43] [44].

Part V.
Detection of Doppler shifted Signals scattered on Airplanes

In the previous chapters EAS, RADAR and meteors were described. In this work a combination of these topics is shown in a study of the feasibility of RADAR detection of EAS by the measurement of radio waves scattered on ionisation trails. The first step in this part was the construction of a test setup for the RADAR detection of airplanes in order to understand the properties of a RADAR setup. The detection of airplanes by the measurement of Doppler shifted radio waves scattered on their metallic surfaces can be used for a demonstration of the capabilities of a passive RADAR setup.

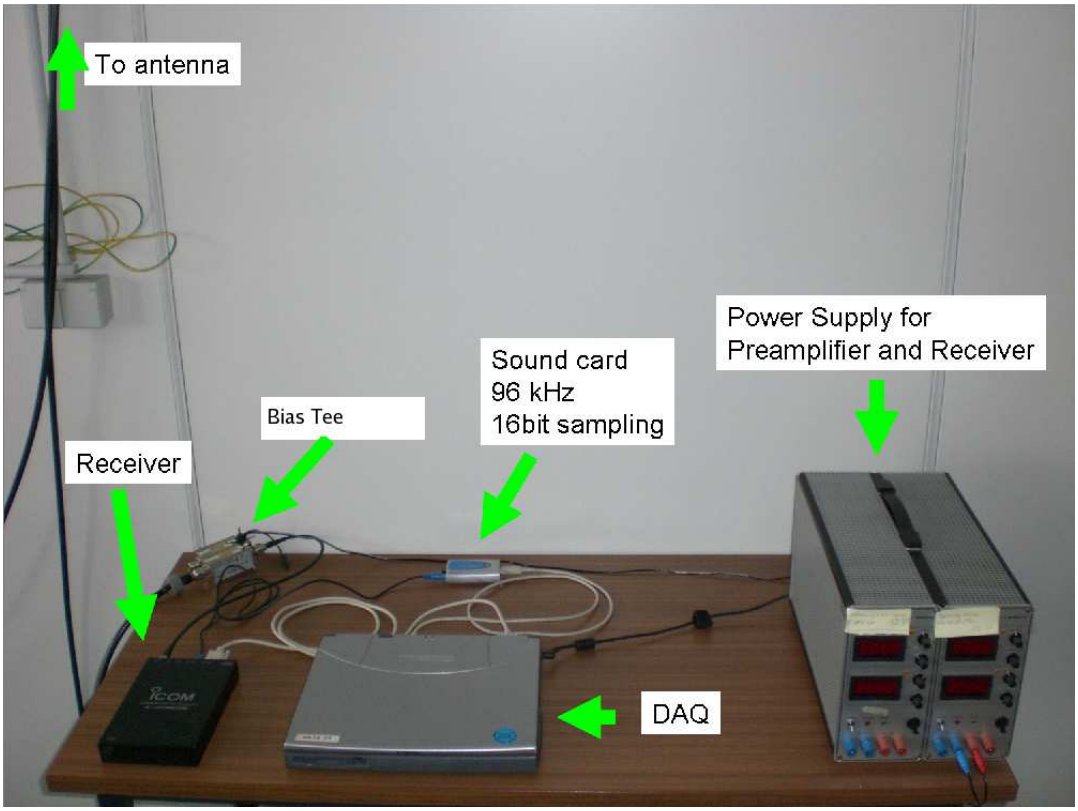

Figure 13: The RADAR measurement setup. The black box in front on the left is the receiver that is connected to the bias tee behind it and from there with a cable to the amplifier and antenna. In the middle is the laptop used to control the receiver and save the wave files. Behind it is the sound card used to digitize the output of the receiver. On the right side is the power supply for the LNA and the receiver in the second part of the measurement.

12. Setup

The setup for the airplane detection is very simple. It consists of an antenna, a radio receiver and a data storage device. A picture of the setup is shown in figure 13. It shows that the setup is small enough to fit on a desk. The receiving antenna is located on the roof of the Physikzentrum in Aachen.

12.1. Antenna

For this part of the measurements we used a log-periodic-dipole antenna (LPDA) mounted on top of the Physikzentrum in Aachen. This specific form is called $LOPES^{Star}$ and was designed at the Forschungszentrum Karlsruhe and built in Aachen.[7] The schematics of the antenna are shown in figure 14 and a picture of the mounted antenna is shown in figure 15. LPDA's are favorable for this kind of measurement because they have a wide field of view upwards along the antenna axis and nearly no sensitivity towards the horizon or the ground. Because of this characteristics man made noise from the horizon is already reduced in the antenna. In addition, LPDA's have a good intrinsic amplification and are designed for wide band reception, which allows the detection of weaker signals on several usable frequencies. The used model had a bandwidth of 40 MHz to 75 MHz, a gain factor of G $\simeq$ 5.5 dBi and a beam width of 50° [45]. An explanation of these antenna characteristics is given in the appendix.

12.2. Amplification and Cables

Directly below the antenna the signal was amplified with a low noise amplifier (LNA) with a bandwidth that was slightly greater than the bandwidth of the antenna [45]. The amplification factor was +20 dB. The receiver was connected with the LNA over 70 meters of RG213 cable. The operation voltage of U = 5 V for the LNA was delivered by a bias tee. With this construction it is possible to deliver the operating voltage over the measurement cable. It works as a frequency filter that separates dc signals like the operating current from high frequency signals like the signals received in the antenna. The used bias tee has a frequency range from 10 MHz to 3000 MHz and a maximum voltage of 12 V.

12.3. Receiver

The used receiver was an ICOM PCR-1000 PC controlled broadband radio receiver[8]. The receiver was used to transform the radio-signals of several megahertz into the frequency range of audible sound waves. This process is called demodulation. Therefore, the receiver was used in the so called continues wave (CW) mode, which is normally used

[7] LOPES, the LOFAR PrototypE Station is a cosmic ray detector array. It is used to show the feasibility of the detection of EAS by measuring radio signals produced by the shower [1]. LOFAR is the LOw Frequency ARray for radio astronomy.

[8] www.icomusa.com

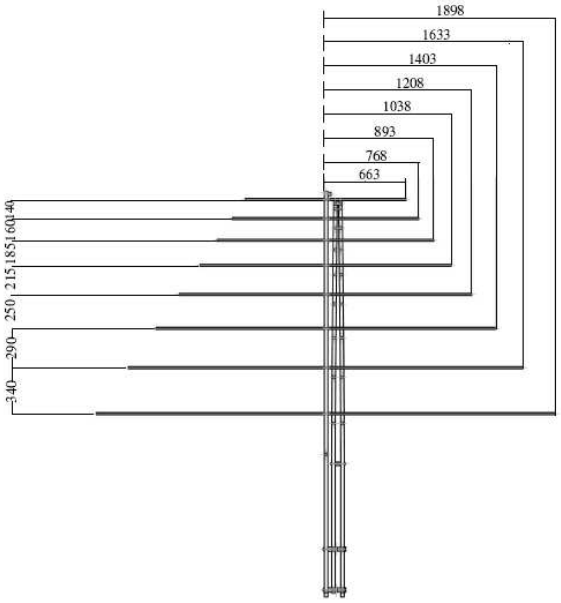

Figure 14: Schematics of the $LOPES^{Star}$ LPDA antenna. The lengths given are the dimensions of the resonant parts of the antenna in mm.

to receive Morse code signals. The signals are transmitted by switching between two unmodulated frequencies separated by several hundred Hertz. In this mode frequencies in the range of audible sound waves are generated by subtracting the dialed-in carrier frequency, so that the sound frequency is the frequency difference between the the received frequency and the carrier frequency. In a second step this signals could be made audible with a sound output device.

An example:

> A carrier frequency of $f_0 = 40\,000\,000$ Hz is chosen. A signal with a frequency of $f_1 = 40\,000\,800$ Hz is received. The output signal would than have a frequency f_2 of $f_2 = f_1 - f_0 = 800$ Hz.

Very low frequencies are not easily resolved by the human ear. Therefore an additional frequency shift is performed in the receiver. After the subtraction of the carrier frequency the obtained frequency is shifted upwards by 700 Hz. The signal from the example would then give an audible tone with a frequency of 1500 Hz.
For the total receiver bandwidth the PCR-1000 has two settings: One with a bandwidth of 2800 Hz and a second with 6000 Hz. The settings of the receiver were controlled by a serial interface with a graphical user interface running on a Windows laptop. A schematic showing the signal flow is shown in figure 16.

12.4. Data Acquisition and Processing

The sound output of the receiver was than digitized with an external M-Audio Travel USB sound card. Sound files were saved in regular intervals on an external storage

Figure 15: Picture of the LPDA mounted on top of the Physikzentrum in Aachen.

device with the software "Spectrum Laboratory"' by DL4YHF [9]. Used settings for the digitization and sound files were a sampling rate of 96 kHz and a sampling depth of 16 bit. Possible file lengths were 60 minutes, 30 minutes and 15 minutes. For the most part a file length of 30 minutes was used. A 30 minute sound file with the above settings has a size of about 330 MB. Data were taken around the clock. Sound card and storage device were connected to the same laptop that was controlling the receiver.
For the data analysis, two dimensional histograms showing the received intensity for a given frequency and time for a whole file were created. All histograms and large parts of the analysis were done with the ROOT framework [46].
To generate these histograms the raw audio data was Fourier transformed.

12.4.1. Fourier Transformation

A method to gain frequency information out of amplitude data is the Fourier transformation. The data were saved in the .wav format, which contains the amplitudes as function of time with a resolution of 96000 samples per second. Amplitude information over time is called time domain. If only some different frequencies contribute to the recorded sound it is impossible to identify these frequencies when looking at the waveform. In order to obtain frequency dependent information, that is intensity as a function of frequency, one has to apply a Fourier transformation on the data.

In order to understand the mathematics of the Fourier transformation one must also understand the sampling process done with the original waveform [47]. The sampling theorem states that only frequencies are sampled correctly which have at least two sampling points in their whole period. That means, that for a given sampling frequency f_s

[9] freenet-homepage.de/dl4yhf/spectra1.html. DL4YHF is a call sign of a ham radio amateur.

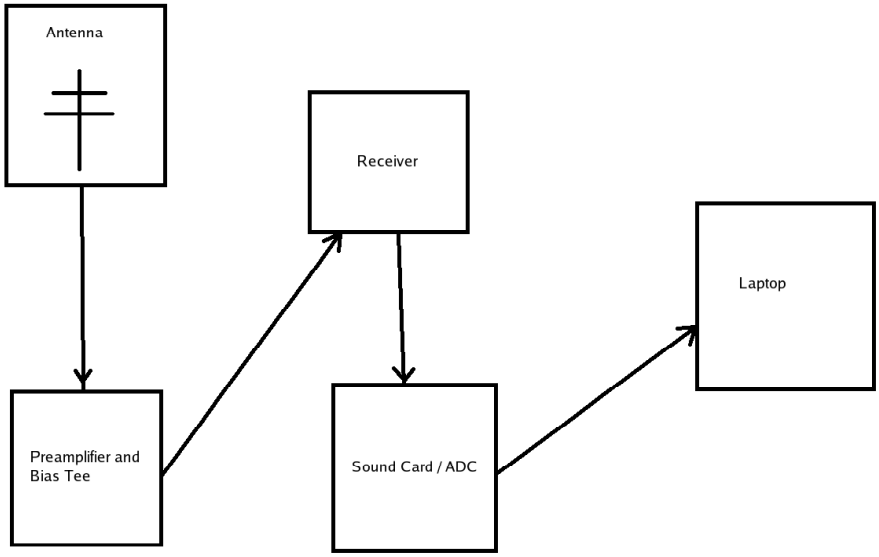

Figure 16: Overview of the different steps of signal processing in the setup

the highest correctly sampled frequency is given by $f_{max} = f_s/2$. In our case, with a sampling frequency of $f_s = 96000\ Hz$ the frequency range from 0 Hz to $f_{max} = 48000\ Hz$ is saved. This frequency bandwidth is far greater than the maximum output bandwidth of the receiver of maximal 6 kHz. This means that frequency information for 6000 Hz to 48000 Hz is saved without any information in it. The high sampling rate of 96 kHz was nevertheless chosen to enable a high time resolution in the Fourier transformation.

The Fourier transformation of the entire data saved in the sound file would give the intensity of the frequencies for the whole time of the sound file. For a Fourier transformation one free parameter is the length of the time domain information. This length is inversely proportional to the frequency resolution of the Fourier transformation. By dividing the data into many sniplets in time the frequency resolution goes down but time information for these sniplets is obtained. The consecutive sequence of frequency information from the sniplets is then the frequency information for the whole data set with a time resolution of the length of the input sniplets.
The sampling theorem and the theory of Fourier transformations describe the properties of the transformation output (see [47]).
A transformation of $2 \cdot N$ sampling values gives $2 \cdot N$ output values. If the input samples f_j are numbered from $j = -N$ to $j = N - 1$, the Fourier transformation can be calculated as:

$$F_K = \frac{1}{2N} \sum_{j=-N}^{N-1} f_j \exp\left(\frac{-2\pi\ i\ jk}{2N}\right) \tag{20}$$

with $k = -N, \ldots, N - 1$. If the input values are purely real numbers, the real and

imaginary parts of the Fourier coefficients can be calculated as:

$$Re(F_K) = \frac{1}{2N} \sum_{j=-N}^{N-1} f_j \ \cos\left(\frac{2\pi\ jk}{2N}\right) \tag{21}$$

$$Im(F_K) = -\frac{1}{2N} \sum_{j=-N}^{N-1} f_j \ \sin\left(\frac{2\pi\ jk}{2N}\right) \tag{22}$$

The output of most Fourier transformation routines contains the real and imaginary part for the output values. The intensity of the Fourier coefficients is than obtained by the addition of the real and imaginary part. The Fourier coefficients with negative indices contain the same information as those with positive indices and are often omitted in the output.

For a given sampling rate f_s we get the time difference between two sampling points x_s by

$$1/x_s = f_s \tag{23}$$

The number of sampled points in the sniplet is given by

$$2N \tag{24}$$

The time length A of the sniplet is then

$$A = 2N \cdot x_s \tag{25}$$

The frequency width of the output values, the so called minimal frequency f_{min} is given by the frequency with one period in the time window A

$$f_{min} = 1/A \tag{26}$$

The maximum frequency was given as

$$f_{max} = f_s/2 \tag{27}$$

These properties can be combined into several general equations:

$$f_{min} = 1/A \tag{28}$$

$$2 \cdot f_{max} = 2 \cdot N \cdot f_{min} = 2 \cdot N \cdot 1/A \tag{29}$$

What we learn from these equations is that better resolution in time means worser resolution in frequency and vice versa. For every transformation we have to choose a compromise between time and frequency resolution.
This explains also the use of a sampling rate of 96 kHz with an audio bandwidth of 48 kHz when the usable bandwidth is only 6 kHz at best. The higher the sampling rate the better the overall resolution of the Fourier transformation output.

Because we were interested only in the intensity of the frequencies we add the real and imaginary part of the Fourier output in squares. This value was then filled into the histogram and plotted. All Fourier transformations were computed with the FFTW library.[10] An example of the output intensity histogram with a time resolution of 1 s and frequency resolution of 1 Hz is shown in figure 17. The visible features are explained in section 13.

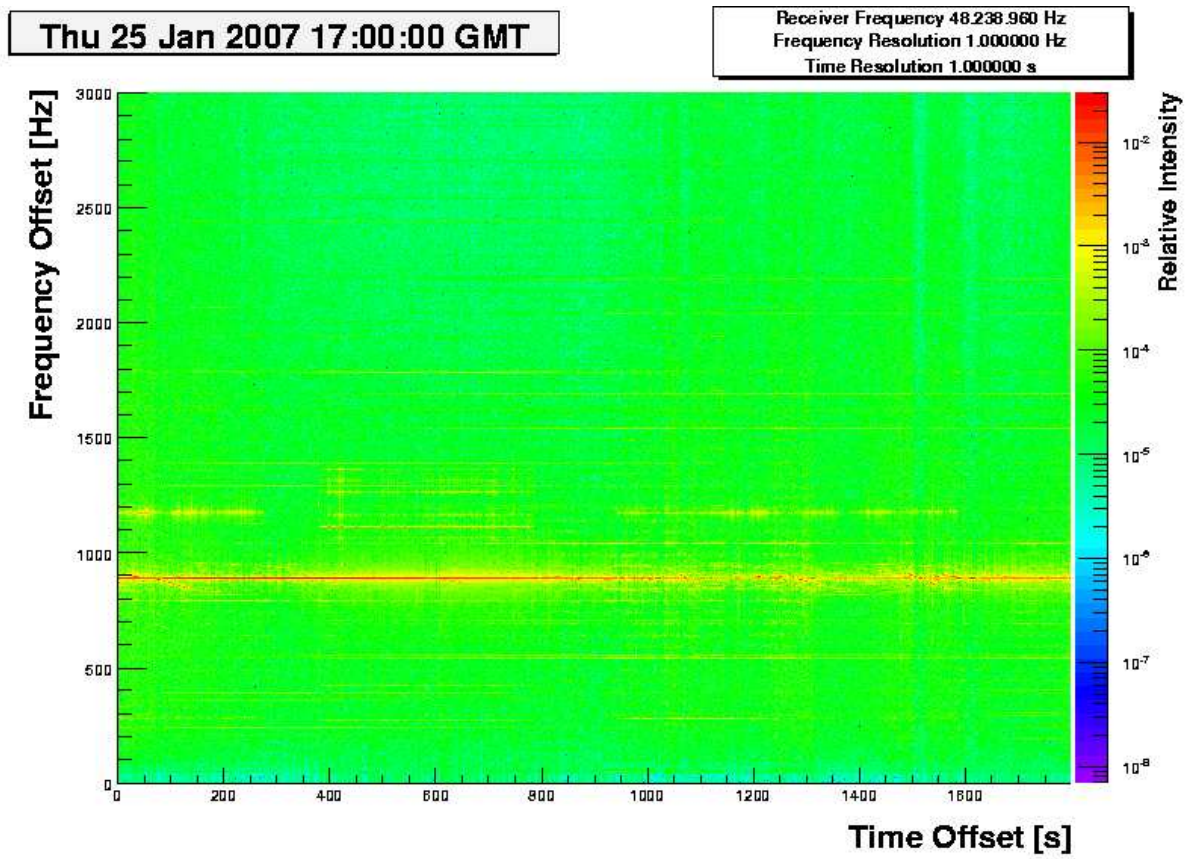

Figure 17: An example of the output of the Fourier transformation showing the intensity color coded over frequency and time.

[10] www.fftw.org

12.5. Transmitters

The first task for our goal of detecting airplanes with a passive RADAR setup was the choice of the transmitter. Possible transmitter classes are TV transmitters, AM radio stations, FM radio stations, static active RADAR transmitters of airports or scientific experiments and ham radio beacons.

- FM transmitters are not used because their transmitting frequency is not constant. They use frequency modulation and so it would be impossible to separate Doppler shifts of the scattered signal from frequency shifts in the transmitter.
- Ham radio beacons are typically tilted towards the horizon and do not illuminate the sky, so their signals can not be reflected at airplanes.
- A good choice would be AM stations, however many AM radio stations in the region are in a process of decommissioning and the remaining few are not in a frequency range where our antenna is sensitive.
- There are no airport RADAR's and scientific RADAR's present in Aachen, so this type of transmitter was also not usable for our measurement.

Because of the relatively low altitude of airplanes ($\sim 11\ km$) compared with micrometeors ($\sim 100\ km$) it is nearly impossible to see reflected signals from a transmitter not in the direct field of view of the receiving antenna. The remaining transmitter type usable are TV transmitters. In the frequency band where our antenna is sensitive there are four different TV channels [48]:

Channel	Frequency Range	Carrier Frequency
E-2	47 MHz - 54 MHz	48,25 MHz
E-2A	48,5 MHz - 55,5 MHz	49,25 MHz
E-3	54 MHz - 61 MHz	55,25 MHz
E-4	61 MHz - 68 MHz	62,25 MHz

Every TV channel is transmitted by a network of transmitting stations. To reduce interference between neighboring transmitting stations, every station is operated with a different frequency offset of the order of 10 kHz.

TV transmitter operate with a modification of amplitude modulation. Amplitude modulation means that the amplitude of a monofrequent carrier frequency is modulated by the signal that is to be transmitted. This modulation introduces additional spectral components in the frequency picture of the transmitter. The resulting frequency spectrum of an AM transmitter is shown schematically in figure 18.

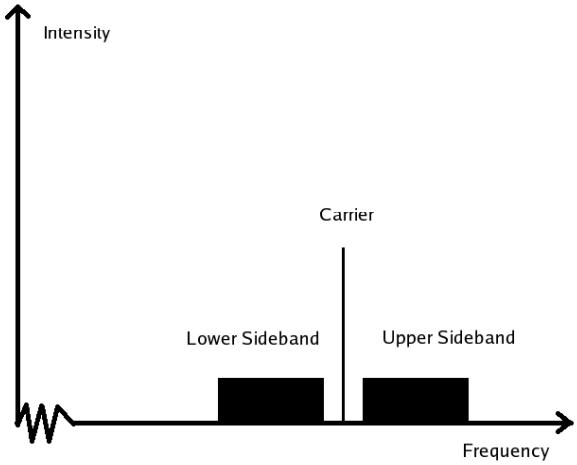

Figure 18: This frequency spectrum of an AM transmitter shows the 3 spectral components resulting from amplitude modulation. In the center we find the unmodified carrier frequency. The block with higher frequency than the center frequency is called upper side band (USB) and is the representation of the modulating signal. The block with lower frequencies than the center frequency is the mirror image of the USB and is called lower side band (LSB).

Amplitude modulation results in 3 spectral components. The first component is the carrier wave with an unmodified frequency. In addition 2 sidebands are introduced, the one with higher frequencies is called the upper side band (USB), the one with lower frequencies than the center frequency is called lower side band (LSB). Both sidebands are mirror images of each other and lie symmetrically to the center frequency. Every sideband is a representation of the modulating signal and contains the whole information of the transmission. One of the sidebands is redundant and is suppressed before actual transmission for TV transmitters. This transmission mode is called single side band (SSB).

The central frequency carries 2/3 of the transmission power, each of the side bands carries 1/6 of the transmission power. In addition the power of the sideband is distributed over a large frequency space compared to the center frequency and the intensity of the frequencies is varying with time. This leads to the effect that for distant transmitters only the carrier frequency is detectable. From long distances AM transmitters look like monofrequent transmitters, the kind of transmitter best suited for our measurements. TV stations transmitting in the frequency band where our antenna is sensitive operate only in southern Germany, far outside our receiving range. Because no lists with transmitter locations and frequencies were obtainable by us, we scanned the whole sensitive frequency bandwidth of our antenna to find a transmitter with a high transmitting power.

We found a reasonable strong transmitter with a frequency of 48237370 Hz. Searches in several (incomplete) lists of transmitters could not identify the exact station. We used the transmitter nevertheless because it turned out to be suitable for a proof of principle measurement. The unknown transmitter location and missing triangulation capability make it impossible to calculate the exact scattering geometry. Nevertheless these measurements are a good training ground for gaining experience in radio signals, transmitter technologies, demodulation, Fourier transformation and the classification of radio noise. It's therefore a suitable testbed for the operation of a bistatic RADAR setup.

13. Results

The airspace above Aachen has a significant amount of commercial airplane traffic. This is explainable by the proximity of several commercial airports, for example in Cologne, Düsseldorf or Maastricht. Sometimes groups of airplanes with nearly similar courses are following one another with a time difference of 2 to 5 minutes which we assume to follow air traffic corridors. Several visual inspections of the air traffic on clear days showed up to 70 airplanes per hour with different courses, speeds and altitudes. Most of the time several airplanes are visible above the antenna.

13.1. Observed Features of Traces

Shown in figure 19 is a zoom in on an output histogram of a measurement taken on the 25th January 2007 between 18:00 and 18:30 local time. The frequency range is centered on the transmitter frequency found in our search. The used transformation parameters were 1 second time resolution and 1 Hz frequency resolution. The receiver frequency was 48.238.960 Hz.

The features visible are:

- The central horizontal line with a frequency of 890 Hz after demodulation. This corresponds to a frequency of 48237370 Hz received in the antenna. This line is the signal of the transmitter found in our frequency scan. It is active all the time and transmitting with a constant frequency.
- The regular broadening and rise in intensity of the central line. We assume that this behavior comes from a local broadband noise source with an on / off behavior and a time constant of about 15 minutes. This noise source is responsible for a small rise in the total noise level of all frequencies between 40 MHz and 80 MHz. This rise in the noise level so small that it is not visible in our representation but the additional received power for the whole antenna bandwidth leads to an overflow in the amplifier and receiver so that already very intense frequencies become broader in frequency [49]. This noise source was already measured by Tobias Winchen [1] in the background measurements for his diploma thesis.

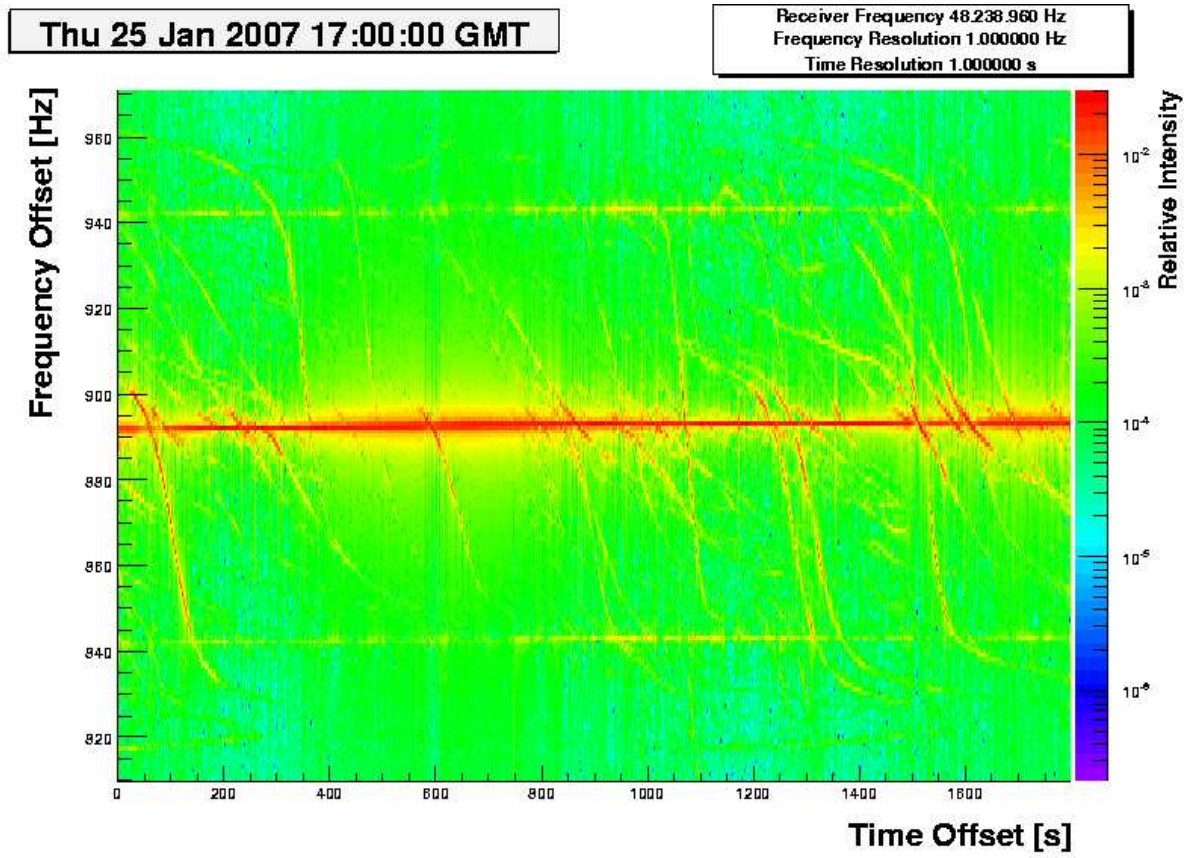

Figure 19: A zoom in on figure 17 centered on the transmitter frequency with an offset of 890 Hz. Visible are the transmitter as horizontal line and trails with changing frequencies.

- The next visible feature are the two horizontal lines at 840 Hz and 940 Hz, exactly 50 Hz above and below the central transmitter frequency. Private communication with ham radio amateurs lead us to the conclusion that these lines result from the use of a TV transmitter as signal source. An explanation for this hypothesis is that TV pictures are transmitted with a frequency of 25 Hz. This additional modulation is not directly visible in the carrier frequency but we assume that after demodulation and Fourier transformation these two "ghost lines" with strongly reduced intensity are found in the output with a frequency difference of two times the modulation of 25 Hz because of sampling effects. This signals are probably not signals received in the antenna but are completely introduced by the Fourier transformation. They are repetitions of the central line. These are repeated with changing intensities but constant frequency differences over a large frequency span, for example visible in figure 17. Because the intensity of the ghost lines is much smaller than that of the original lines only very strong signals produce ghost lines. We checked for this behavior with other transmitter types, but only TV transmitters showed these kind of mirror images.

- The feature most relevant for our RADAR investigation however are the lines crossing the central line beginning with higher frequencies than the central line and ending with lower frequencies than the central line.

A zoom in on the first 400 seconds of the data (figure 20) shows some of these traces in greater detail. Their characteristics are:

- All traces start with a frequency higher than the central line and end with a frequency lower than the central line.
- The traces can have a different:
  - duration
  - steepness
  - position with respect to the central line.
- All traces have roughly the same intensity profile: Low intensity at start and end of the trace and higher intensity in the middle. All traces have a maximum in intensity when crossing the central line.
- Sometimes groups of traces with similar shapes are visible separated by several minutes.
- An upper and lower limit for the frequency difference between the trails and the central line exists.

We assume that these traces are the result of radio wave scattering on moving commercial airplanes. With this hypothesis it is possible to explain the observed features of the trails. The effect producing the characteristic shape of the trails is the bistatic Doppler shift.

13.2. Interpretation of Features as Airplane Reflections

An explanation of the observed features with the assumption of commercial airplanes as scatterers:

- The fact that all traces begin with higher frequencies than that of the transmitter is due to the scattering geometry and the opening angle of our antenna. All airplanes that are visible for our antenna must enter the antenna field of view from the outside. That means that at the time of first reception all airplanes have a velocity that is directed towards the receiving antenna and the stationary transmitter in the field of view of the antenna. Motions that lead to a shrinking in the bistatic range sum result in a higher frequency than the original transmitter frequency as shown in section 8.2. This leads to the typical form of the airplane trails, beginning with the highest frequency when their movement reduces the bistatic range sum, reaching a point where the range sum is minimal and the

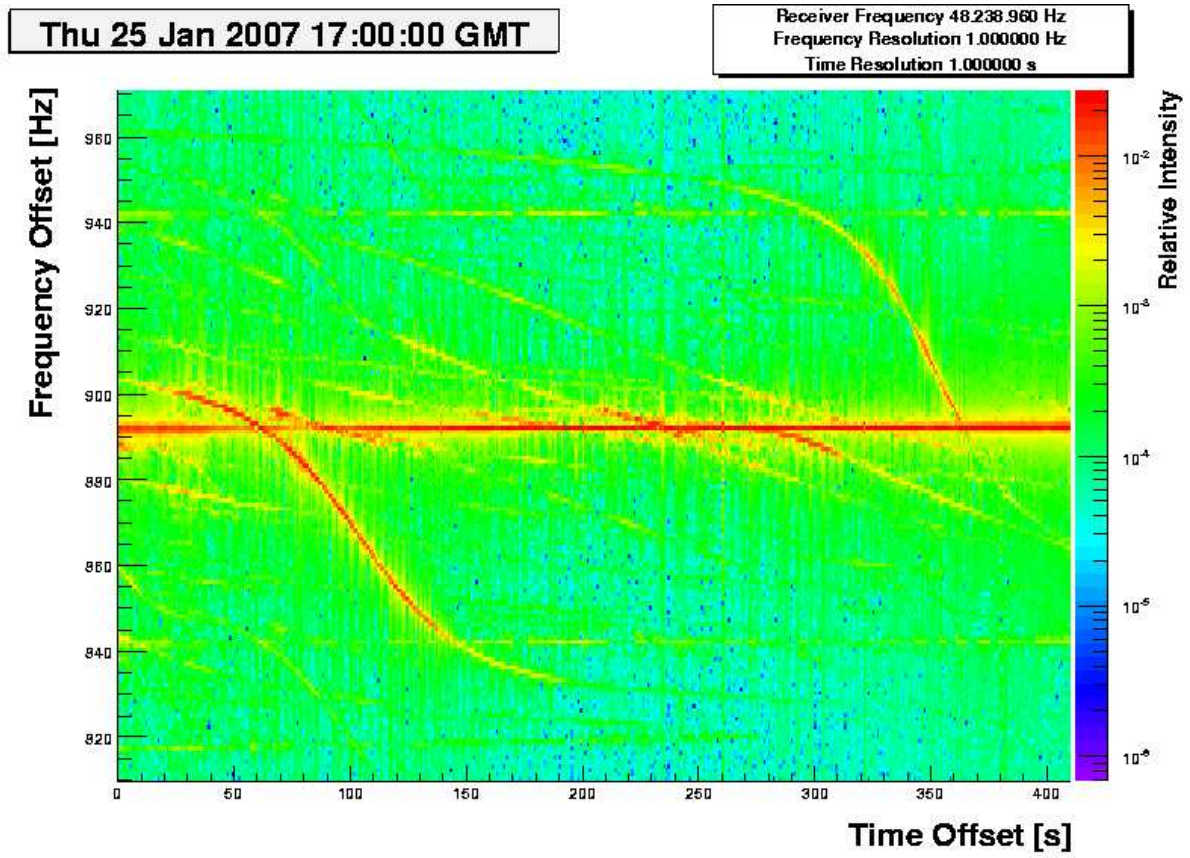

Figure 20: The first 400 seconds of figure 19.

Doppler shift is zero. After reaching this closest point the range sum becomes larger with time, leading to lower frequencies. The traces end when the airplanes leave the sensitive area of the antenna.

- The different shapes of the traces are due to the different geometries for every airplane. The geometries differ because every airplane crosses the field of view of our antenna at a different altitude, at a different distance and with a different velocity. The velocity visible in the bistatic Doppler shift is the radial projection of the airplane velocity towards the transmitter and receiver. Different geometries lead to different time development of the airplane position and so to different shapes of the trails.

- The intensity development for each trail is governed by the $1/R^2$ terms in the RADAR equation (equation 12), leading to lower intensities at the starting and ending points of the trail because R_R and R_T are both large and higher intensities in the middle of the trail when these ranges are small. The maximum in intensity occurs for the point of minimal bistatic range sum. At this point the bistatic Doppler shift is zero, leading to the point where the trails cross the central line. The second effect changing the received intensity is the relative scattering area

on the plane (the RADAR cross section - RCS) dependent on the aspect angle from the transmitter and receiver and the form of the airplane. RCS values for commercial airplanes range from 5 m^2 to 20 m^2 [35]. The calculation of the RCS of an airplane for different aspect angles is not possible for us.

- The existence of an upper limit for the frequency difference between the trails and the central line is explainable by the maximum velocities reachable by airplanes. Commercial airplanes have a maximum velocity between 800 km/h and 1000 km/h.
  The points of maximum bistatic range sum visible for our setup are the starting or the end point of the trail and are identified by the maximum relative frequency difference to the original frequency. Because of the long range and small aspect angles at these points the visible relative velocity is a lower bound for the velocity of the airplane. This velocity can then be calculated with equation 17. For these long distances the velocities towards the receiver and transmitter are assumed equal. There are several traces with a maximum visible Doppler shift of +70 Hz or -60 Hz. The majority of traces has maximum frequency differences that are slightly smaller. Inserting a Doppler shift of 70 Hz and the transmitter frequency of 48.238.960 Hz into equation 17 gives a velocity of 216 m/s or 783 km/h. That is in the same order of the maximum velocity reachable by airplanes. That not all lines have such high velocities is explainable by the relative low distance from our receiving antenna to the airports in the vicinity (around 100 km for the airport in Cologne) meaning that many airplanes do not travel with their maximum speed but have slowed down in preparation for landing.

- Some traces with kinks in their shapes are explainable as a result from a change in the velocity or course of the airplane.

Several trials to match visually observed airplanes with traces found in the data were unsuccessful. This can explained by the geometry of the scattering setup. For the visual observation the time information and courses of airplanes were recorded for a point directly above the receiving antenna. The point that defines the scattering geometry is the point where the bistatic range sum is minimal. Because the transmitter location is unknown and the point of minimal bistatic range sum is different for every airplane and not directly above the antenna for most airplanes the visual and RADAR detected airplanes cannot be matched.

13.3. Analysis of Track Abundance over time

In figure 21 we show the variation in the number of airplane traces for a 48 hour period. The number of airplane traces per half hour interval was counted. An airplane trace was defined as a trace longer than about 20 seconds, a frequency difference with respect to the central line of more than 10 Hz on one side of the central line. In addition an airplane trace had to continue without breaks from its starting point to its end.
We see a clear dependence between the time of day and the number of measured traces.

This is explainable by our hypothesis that these traces are caused by airplanes. The periods with a low number of traces correlate with no flight periods at airports during the night. In figure 22 two examples from the analysed time period are shown, one from 16:30 to 17:00, the other from 4:00 to 4:30.

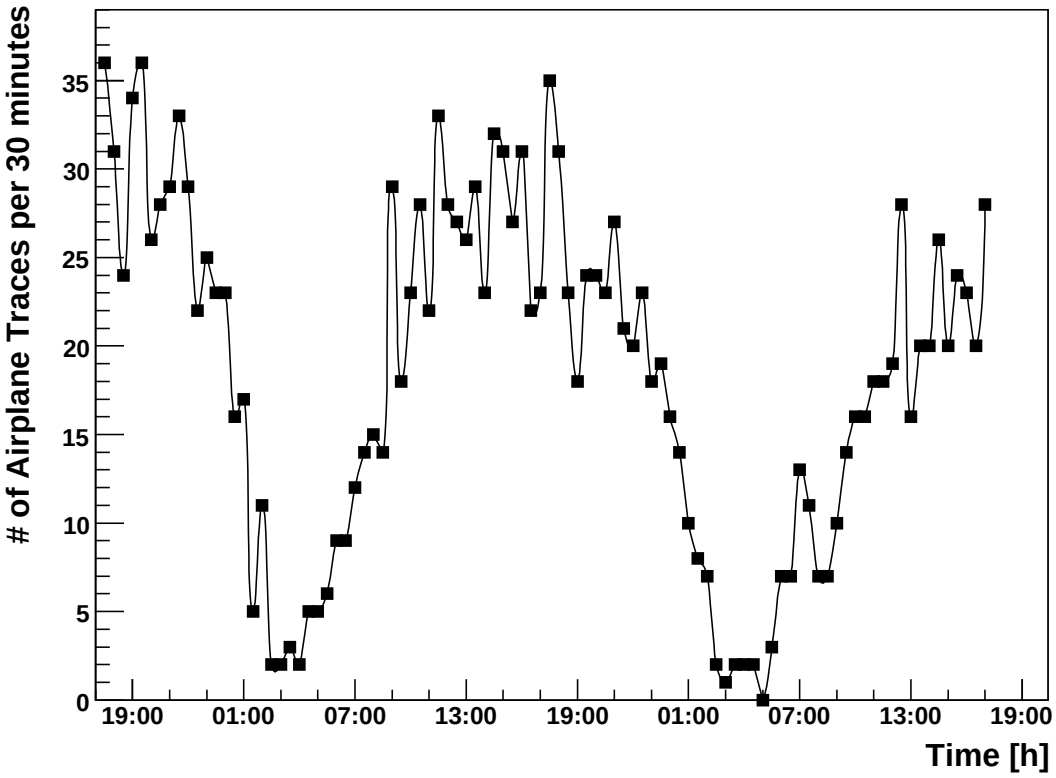

Figure 21: Variation in the number of airplane traces counted in half hour intervals for a time window of 48 hours. Data was taken from 01/25/07 19:00 to 01/27/07 19:00 local time.

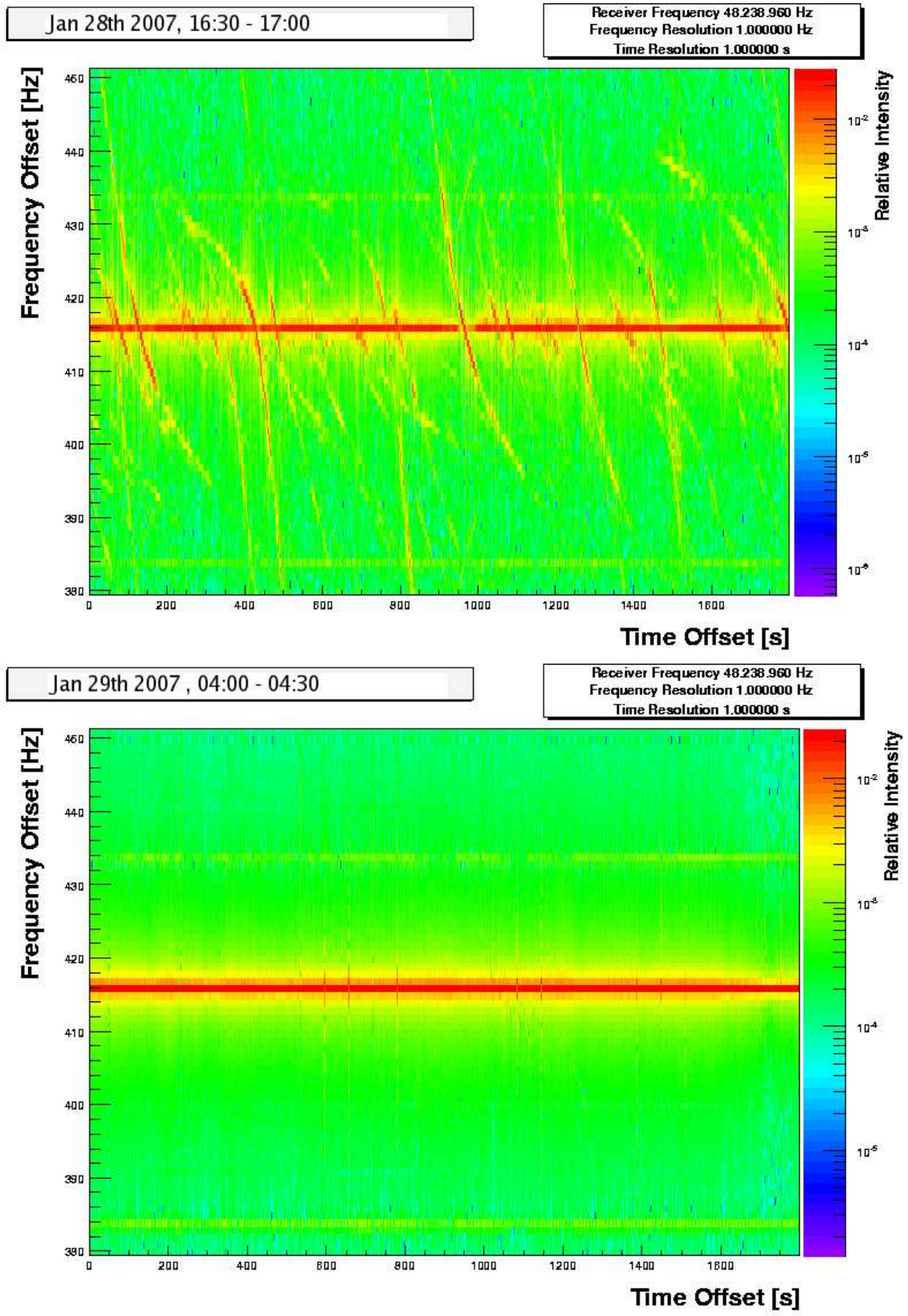

Figure 22: Examples of two time periods with different trace abundance. At the top the time interval from 16:30 to 17:00 is shown. At the bottom the time interval from 4:00 to 4:30 is shown.

13.4. Calculated Traces

Because of the missing information of the airplane position, the transmitter location and RADAR cross sections of different airplanes, a calculation of these features is not possible. However the principle properties were reproduced in a simulation. An example of a calculated Doppler trace is shown in figure 23 to 26. The geometry was defined by setting the receiving antenna in the center of the coordinate system and the transmitter at a distance of -20 km along the x-axis. The transmitter frequency was set to 48.238.960 Hz. We assumed an airplane traveling at a constant altitude of 10 km with a constant velocity of 900 km/h (250 m/s), combined of a motion with of 878 km/h (244 m/s) in the direction of the x-axis and 200 km/h (56 m/s) in the direction of the y-axis. In addition we assumed a distance of 15000 m in x and 13000 m in y direction in the transmitter - receiver plane for the airplane at time t=0. Shown in the figure is the bistatic Doppler shift, the bistatic range sum and the distances from the airplane to the receiver and transmitter.

The resulting trace resembles clearly some of the traces found in figure 19. It is possible to recreate most of the types of traces found in our data by modifying the values for the velocity components and minimum distances of the airplane.

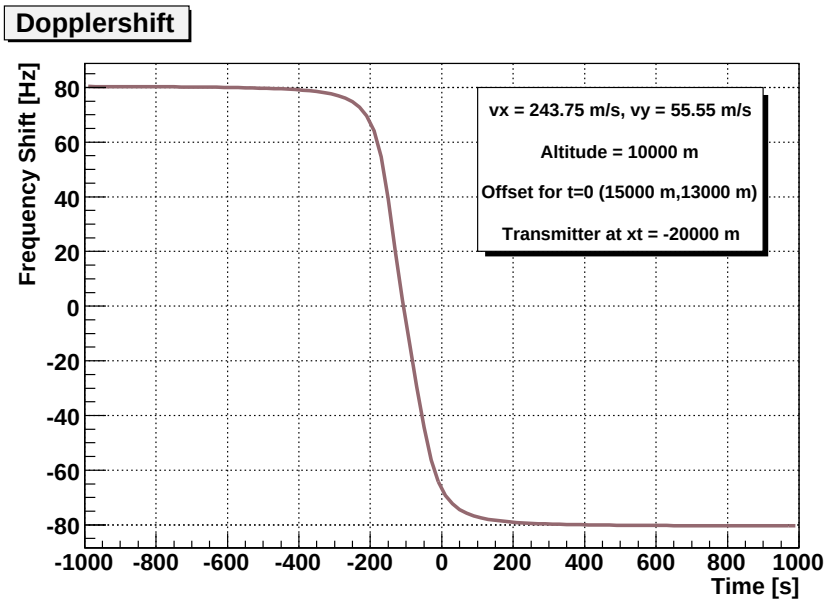

Figure 23: Calculated bistatic Doppler shift for an airplane with a velocity of 900 km/h for a frequency of 48.238.960 Hz. The used values are found in the text.

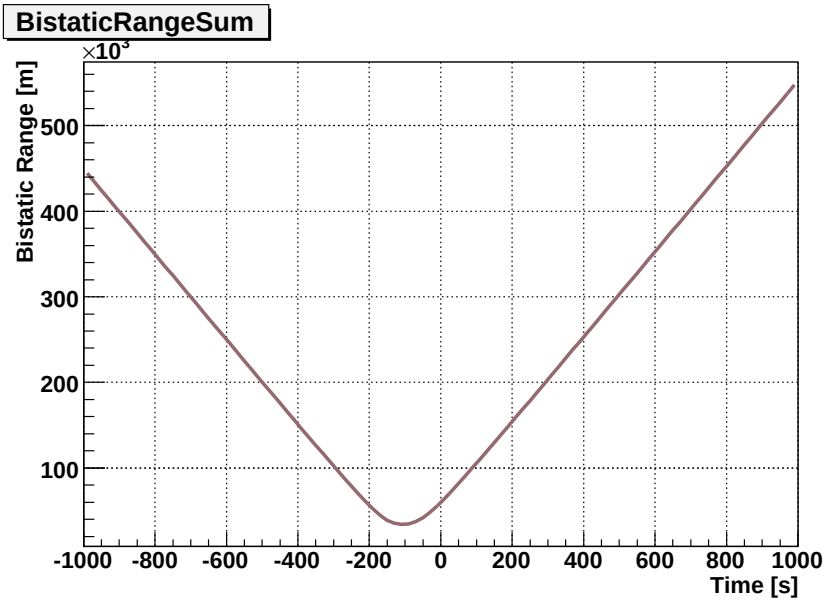

Figure 24: Calculated bistatic rang sum for an airplane with a velocity of 900 km/h for a frequency of 48.238.960 Hz. The used values are found in the text.

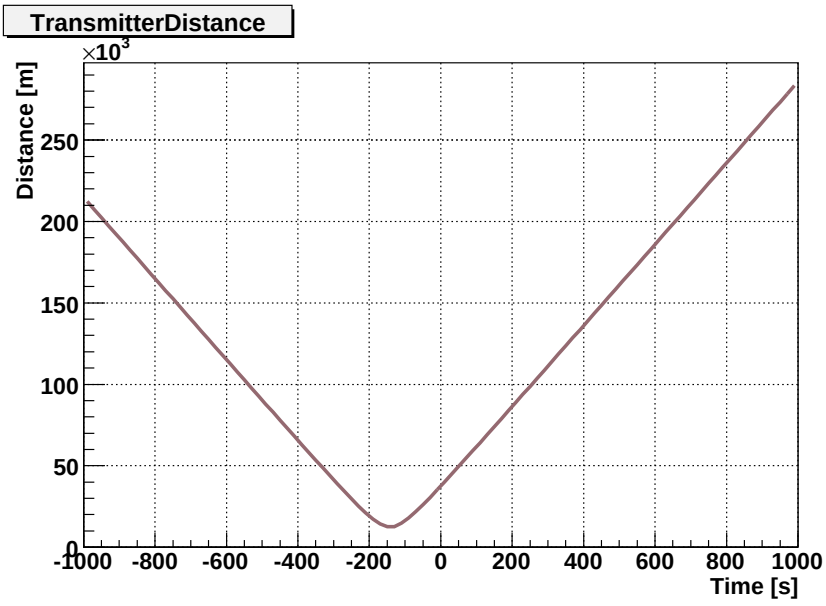

Figure 25: Calculated transmitter distance for an airplane with a velocity of 900 km/h for a frequency of 48.238.960 Hz. The used values are found in the text.

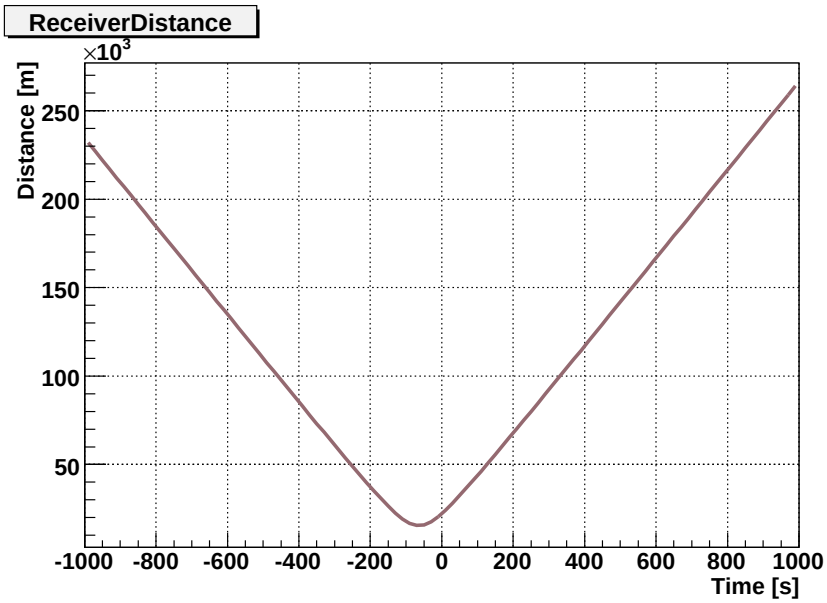

Figure 26: Calculated receiver distance for an airplane with a velocity of 900 km/h for a frequency of 48.238.960 Hz. The used values are found in the text.

14. Conclusion

We assembled a setup for parasitic passive RADAR observation mostly from off the shelf components. The analysis of received signals showed that the setup is capable of observing RADAR for airplanes. We showed that it is possible to explain the measured traces with Doppler shifted signals from commercial airplanes. The next step after this proof of principle is the detection of signals scattered on ionisation columns generated by meteors.

Part VI.
Meteor Scatter

After the detection of signals scattered on airplanes the next step was to detect radio signals scattered on ionisation trails generated by meteors. Goals of this measurements were the identification of meteor scatter signals, the measurements of the diurnal variation in counting rates and the measurement of meteor showers. An analysis code was developed to identify and count meteor scatter signals.

15. Setup

For the detection of meteor scatter signals the setup used to detect signals scattered on airplanes was modified because the scattering geometry for meteors is different than that for airplanes. The different altitudes ($\sim$ 11 km for airplanes, 70 km to 120 km for meteor ionisation trails) result in a much larger base length of the scattering setup. Because the expected signals are very weak we need a transmitter not in the direct field of view of our antenna.

15.1. Transmitter

We searched for a transmitter with a distance greater than 700 km to our reception point. The continued use of a TV transmitter on such distances is not possible anymore because TV transmitters do not illuminate a large enough part of the sky. TV transmitters are normally focused onto the ground, sky illumination is only happening close to the transmitter. In a beacon list regularly published in the magazine "Dubus" [50] we found two ham radio beacons located in southern Norway. These beacons use continuous transmission and have their main transmission direction southwards. Unfortunately the transmission frequency lies in the 2 m band, that is the frequency range from 144 MHz to 146 MHz. The antenna used to detect signals scattered on airplanes is not sensitive in this frequency range anymore. In addition the transmission power of the beacon is very low compared to that of a TV transmitter, resulting in the need for an antenna with high directivity and gain.

Figure 27: A Google Earth map showing the location of the transmitter and receiver of the detection setup [51].

The characteristics of the two beacons are as follows:

Identification	LH3VHF	LH8VHF
Frequency	144.478 MHz	144.480 MHz
Wavelength	2.07500 m	2.07498 m
Location	50° 46′ 54″ N 6° 02′ 56″ E	58° 58′ 45″ N 9° 57′ 20″ E
Distance to Receiver	811 km	946 km
Bearing from Receiver	5°	13°
Transmission Power	120 W	100 W
Transmission Direction	180°	150°

From these two beacons only LH3VHF was used because it has a higher transmission power. A Google Earth map showing the transmitter and receiver location is shown in figure 27.

15.2. Antenna

Because the antenna used to measure signals scattered on airplanes is not sensitive in the frequency range of the radio beacons a different antenna was used. The used antenna was an optimised Yagi-Uda antenna for the 2 meter ham radio band, usable in a frequency range of 144 MHz to 146 MHz. It consists of a 6.5 meter long structure

on which 13 directional elements, one active element and one reflecting element are mounted.Such an antenna is only sensitive in the direction of the long structure and has a relative small field of view compared to the LPDA. It was mounted on the roof of the Physikzentrum in Aachen with a bearing of ca. 10° and looking slightly above the horizon. The transmitter lies below the horizon, so scattering objects have to be only a small angle above the horizon for the used scattering geometry. The antenna has a calculated maximum gain of G=15 dB, and a half power beamwidth of 33°. A schematic view of the antenna is shown in figure 28 and a picture of the mounted antenna is shown in figure 29.

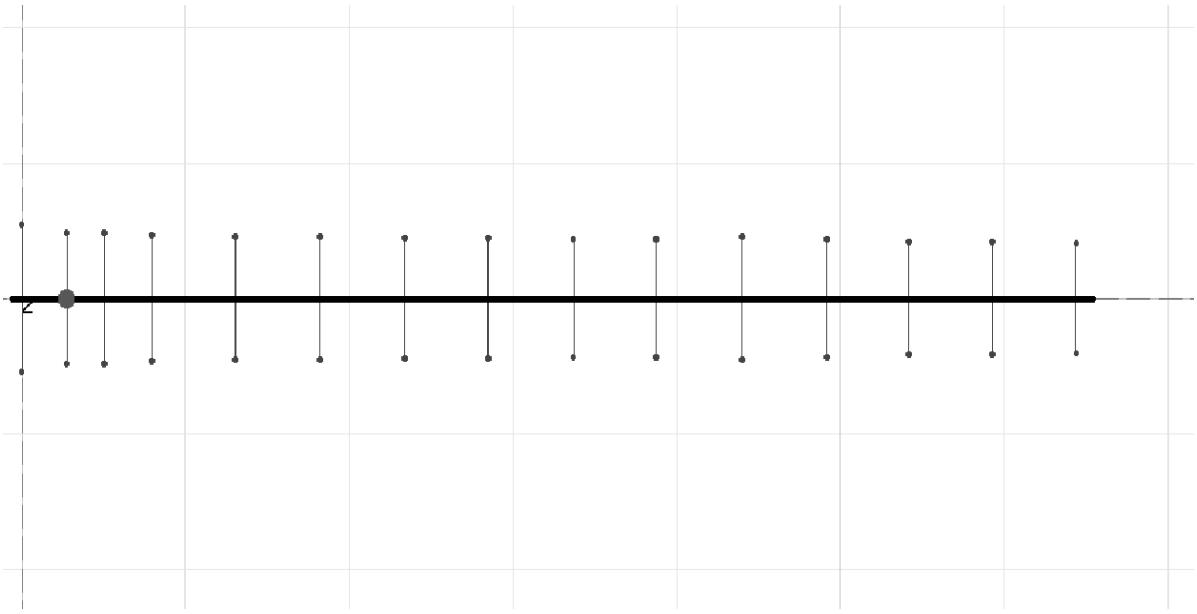

Figure 28: An schematic overview of the used Yagi Antenna, optimized for high directivity and gain in the 2m band (144 MHz to 146 MHz). The receiving element is the second element from the left. All other elements are only used to define the directivity of the antenna. The sensitive direction is shown to the right. The antenna was designed and constructed by Uli Hacker - DK2BJ.

15.3. Amplifier

The used low noise amplifier (LNA) was a BFT66-GK with an amplification of A = 11 dB and and a noise value of NF = 1 dB. The usable frequency range is 100 MHz to 450 MHz. It was located directly under the antenna and before the 70 m cable leading to the DAQ. The operation voltage of U = 12 V for the LNA was delivered by the same bias tee as in the airplane part of the measurement. The same cable as in the airplane part of the measurement was used to link antenna, LNA and receiver.

Figure 29: Picture of the 2 m band antenna mounted on top of the Physikzentrum in Aachen.

15.4. Receiver

Because of problems with transient noise using the PCR-1000 receiver we switched to an "ICOM IC-706 MKII G" receiver with a specially filtered power supply "ICOM OPC-639 DC cable with EMC filter". It has basically the same characteristics as the old receiver but a much lower sensitivity to sparks and power spikes in the electrical system. The used receiver bandwidth was 3 kHz. As demodulation mode USB (Upper Side Band) was used. That is basically the same as the CW mode but with an additional frequency shift of 1 kHz done in the receiver (see section 12.3). To reduce confusion all frequencies that had to be measured were corrected by this offset to allow comparisons between the two receivers (a frequency of 144.414 MHz on the PCR-1000 had to be 144.413 MHz on the IC-706).[11]

15.5. Data Acquisition

Data acquisition worked the same way as in the airplane part. Half hour wave files with 96 kHz sampling rate and 16 bit sampling depth were saved. From these files intensity histograms were generated the same way as described in section 12.4.

16. Data Analysis

16.1. Data Set

Data taking started on the June 29th 2007 16:30 local time (14:30 UMT) and lasted until August 15th 2007 14:30 local time (12:30 UMT). In this time of 1126 hours 1619 half hour wave files were recorded, covering 809.5 hours, that is nearly 71.9 % of the whole data taking period. Downtimes result from power outages, hardware failures, maintenance operations on the receiving setup and discarded files because of active pulsed transmitter signals.

There were several meteor showers with moderate or higher activity classified by "Meteorshowers online"[12] peaking with their activity in this time window:

The Southern Delta Aquarids (SDA), a moderate shower with activity from July 14 to August 18 and a peak time of July 28/29.

The Southern Iota Aquarids (SIA), a moderate shower with activity from July 1 to September 18 and a peak time of August 6/7.

The Alpha Capricornids (CAP), a moderate shower with activity from July 15 to September 11 and a peak time of August 1/2.

The Northern Delta Aquarids (NDA), a moderate shower with activity from July 16 to September 10 and a peak time of August 13/14.

The strongest shower in the data taking period are the Perseids, a major shower with activity from July 23 to August 22 and a very sharp maximum at August 12/13.

[11] The antenna, the receiver and the LNA were borrowed to me by a member of the local ham radio community, Uli Hacker - DK2BJ.

[12] http://meteorshowersonline.com/ by Gary W. Kronk

At least the maximum of the Perseids should be visible in our data by a rise in counting rates for dates around the maximum. The visibility of the other showers was unclear beforehand because of their broad and not very high maxima.

16.2. Event Selection

A first step to the automated processing of the data files was the identification of possible meteor scatter signals in the data set. This was done by listening to the audio files and comparison with meteor scatter examples given to me by ham radio amateurs [49][52]. Meteor scatter signals have a special sound profile. When using signals from a monofrequent transmitter the scattered signals are again monofrequent. A small broadening of the original frequency by the scattering process cannot be resolved by the human ear. It follows that meteor scatter signals sound like a monofrequent tone and not like a noise composed of several frequencies. Characteristic for meteor scatter signals is a fast rise in signal intensity and and exponential decline of intensity. Meteor scatter signals are best found by listening for monofrequent sounds that appear suddenly and become quieter with time. Sometimes the frequency of the sound is changing over time. This effect is produced by Doppler shift when the ionisation trail is moving. For some signals a periodic modulation of the intensity of the sound is found. This leads to a ringing sound effect but is difficult to detect. An explanation for this effect is the interference of radio waves scattered on different points of the trail.
This special sound profile makes them relatively easy to find with some training when listening to them. By listening to several hours of data several signals were found. These signals were confirmed to be meteor scatter signals by radio amateurs [49][52]. For the so found signals the amplitude and frequency characteristics were calculated. A method to allow the automated search for the expected signals was developed based on the signals found by listening.

Most promising was an algorithm that scanned the generated frequency histograms. The expected signals are characterised by their frequency width and their time length. The expected duration of an ionisation column that enables radio wave scattering is 0.01 s to 20 s. Because we use a monochromatic transmitter for the measurement the scattered signals should be small in their frequency range compared to transient noise or spark signatures that can span the whole receiver bandwidth of 3 kHz.

The search strategy was as follows: In a small part of a histogram, consisting of a rectangle with a predefined time length and frequency range the mean and standard variation of the received intensity is calculated. In a second step the intensity in the center of the histogram is calculated for a smaller box inside the first box. The dimensions of this inner box are again predefined and are of the order of the frequency range and duration of the expected meteor scatter signals. If the mean intensity of the inner box is higher than a predefined threshold calculated from the mean and deviation of the outer box this part of the histogram is considered a possible signal. When a possible signal is found the time and frequency information of the outer box together with a sub histogram of the box are written into a root file. After that the starting frequency of

the outer box is increased by one unit and the intensity comparison starts anew. When the whole frequency range was analysed the starting frequency is reset to the lowest possible value and the starting time is increased by one unit. This procedure repeats until the whole histogram is analysed. Because of this procedure it is possible to find the same signal within several steps of the analysis. These double findings are eliminated by merging of signals with overlapping outer boxes. This is done by generating a new outer box with the dimensions from the minimum and maximum dimensions of the two original boxes. This is done until no overlapping of signals is found. The merged signals and those that do not overlap at all are then written into a root file. The result is a root file for every wave file that was recorded. In these root files the found signals are stored as small histograms and identified by their lower and upper frequencies and starting and ending times.

The use of the intensity comparison is motivated by several causes:
The local calculation of the threshold allows the use of the algorithm even in cases where the noise level of the measurement is changing with time or frequency. Signals generated by transient noise are rejected because of their frequency structure. Their frequency range is larger than the expected signals and so larger than the used inner box. That means that the intensity of the bins in the inner box is the same as that of bins in the outer box. It follows that this kind of signals do not register in the intensity comparison trigger. The same is true for signals generated by transmitters in the direct field of view. These signals are rejected because they are much larger than the expected meteor scatter signals. Another type of false positive signal are signals generated by pulsed or Morse code transmitters, in general transmitters with an on - off behavior. Because of the constantly changing received intensity our signal finder will trigger these signals almost every time. To reduce the false positive counting rate, the frequency range in which the signal finder works can be limited, so that only the range where meteor scatter signals are expected is analysed. If by chance a pulsed transmitter is active in the limited frequency range the whole data file is discarded when more than 1000 hits per half an hour wave file are found. The frequency range for the algorithm was limited from 400 Hz to 1000 Hz because the actual transmitter would be received with a frequency of 700 Hz and no signals with frequency differences greater than 300 Hz were expected.

The analysis of the whole dataset was done with several different selection sets. Subsamples of 250 example signals were eye scanned to find the best event cuts. The best results were obtained for an outer box dimension of 1.5 s and 400 Hz and an inner box dimension of 0.3 s and 40 Hz centered in the outer box, both for a time resolution of the Fourier transformation of 0.1 s and 0.05 s. A box was classified as signal, when the mean intensity of the inner box I_{mi} was greater than three standard deviations σ_o above the mean intensity of the outer box I_{mo} :

$$I_{mi} > I_{mo} + 3 \cdot \sigma_o \tag{30}$$

With this value around 7500 signals are found. Larger values of the cut parameter reduce the number of false positive signals but the effect on the meteor scatter signals is far larger.

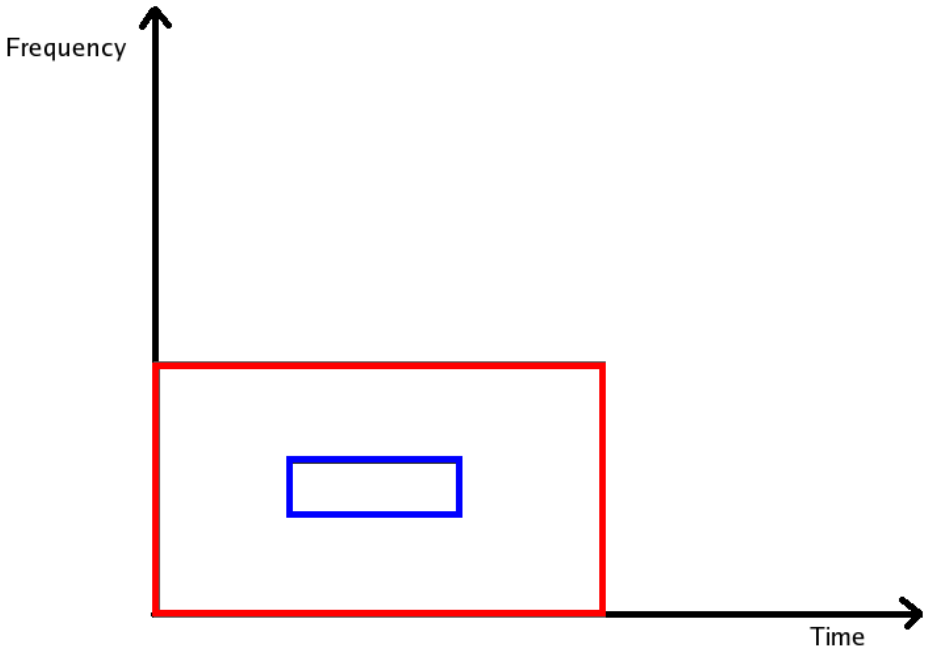

Figure 30: A schematic showing the intensity comparison process. Shown are the borders of the first outer in red and the first inner box in blue.

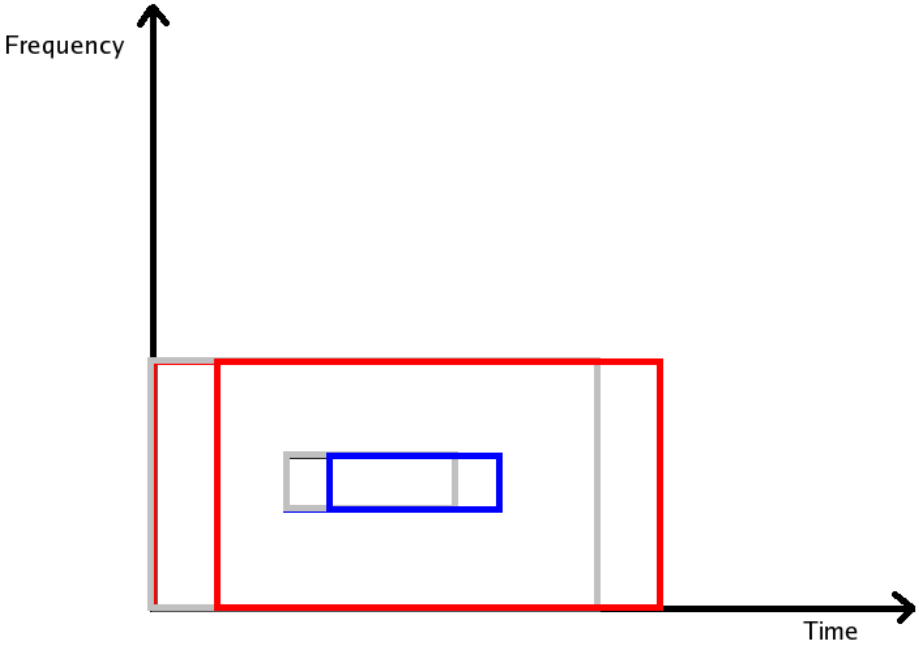

Figure 31: The second step of the intensity comparison process. The borders of the old inner and outer box are shown in grey. The borders of the new outer and inner box are shown in red and blue.

17. Results

Our hypothesis is that the received signals originate from the scattering of radio waves from ionisation columns produced by meteors. Several analysis support this hypothesis.

17.1. Examples of detected Signals

In figures 32,33,34 and 35 we show typical events found by our filter. The upper histogram shows the intensity as function of time and frequency. The range of the x axis is the length of the outer box after signal merging. The frequency range shown is the whole frequency range analysed by the algorithm. The lower histogram shows the summarized intensity as a function of time. The signals shown in figure 32 and 33 are typical examples of meteor scatter signals. They are characterized by their sharp rise in intensity at the beginning and an exponential decline in intensity over time. The signal in figure 34 shows a detected signal without a sharp signal rise and exponential decline. This signal was found to be a meteor scatter signal by showing the typical sound profile when listening to it. The signal in figure 35 shows a typical broad band noise signal that was found as false positive by the analysis. The intensity fills the whole frequency range of the analysis and it has a complicated time structure. Similar signals could be produced by switching on the room light in rooms located close to the DAQ. This leads to the conclusion that this class of signals are produced by switching sparks of electrical devices.

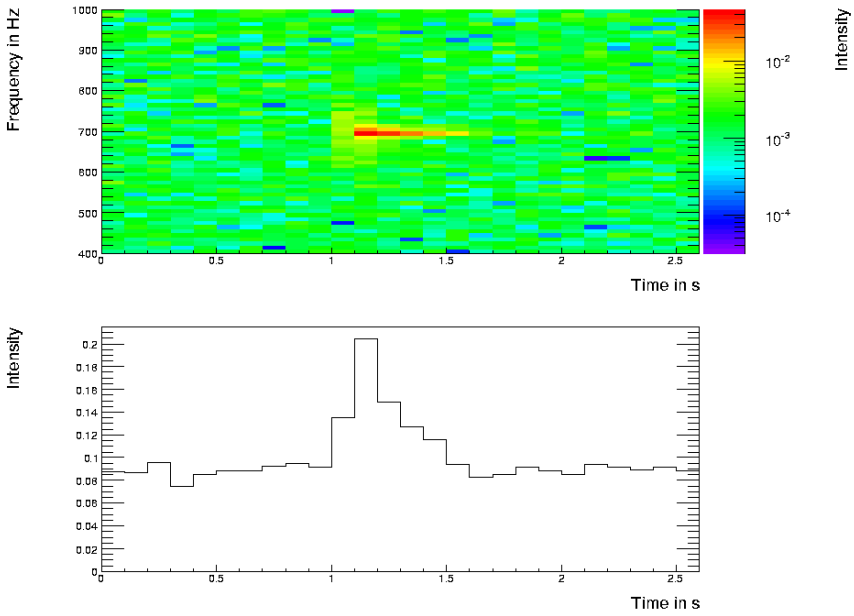

Figure 32: Example signal found in the analysis. Classified as meteor scatter signal. Time resolution 0.1 s.

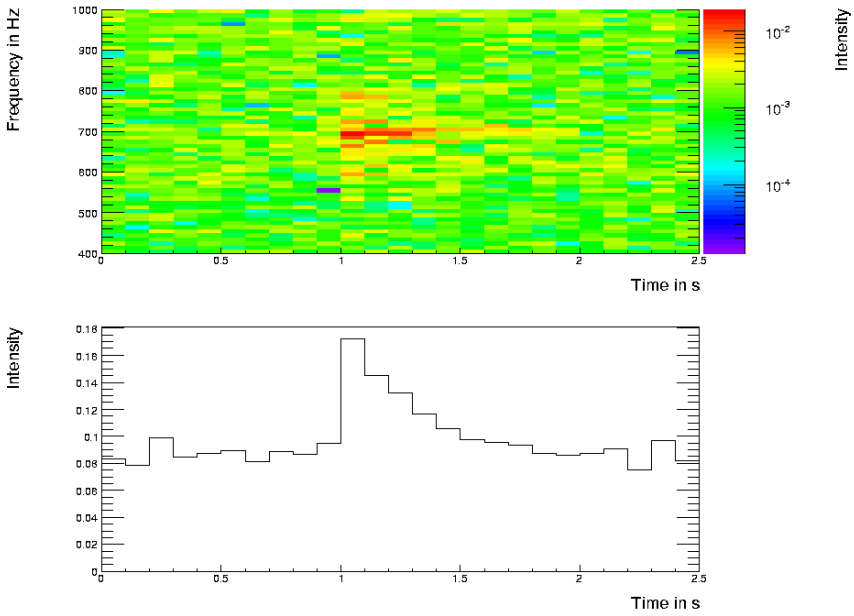

Figure 33: Example signal found in the analysis. Classified as meteor scatter signal. Time resolution 0.1 s.

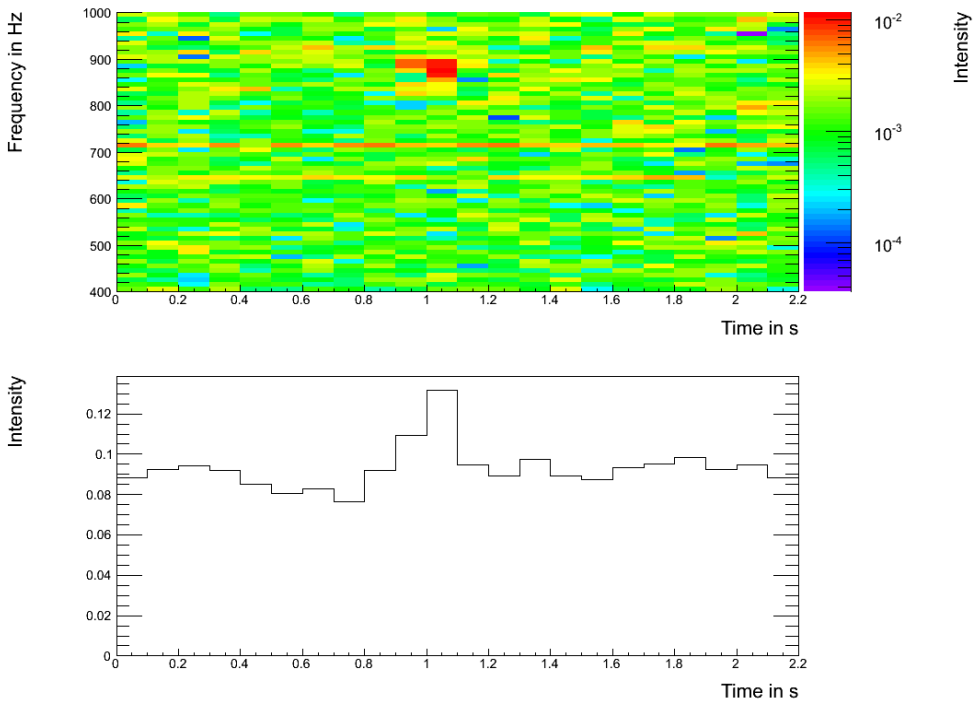

Figure 34: Example signal found in the analysis. Time resolution 0.1 s.

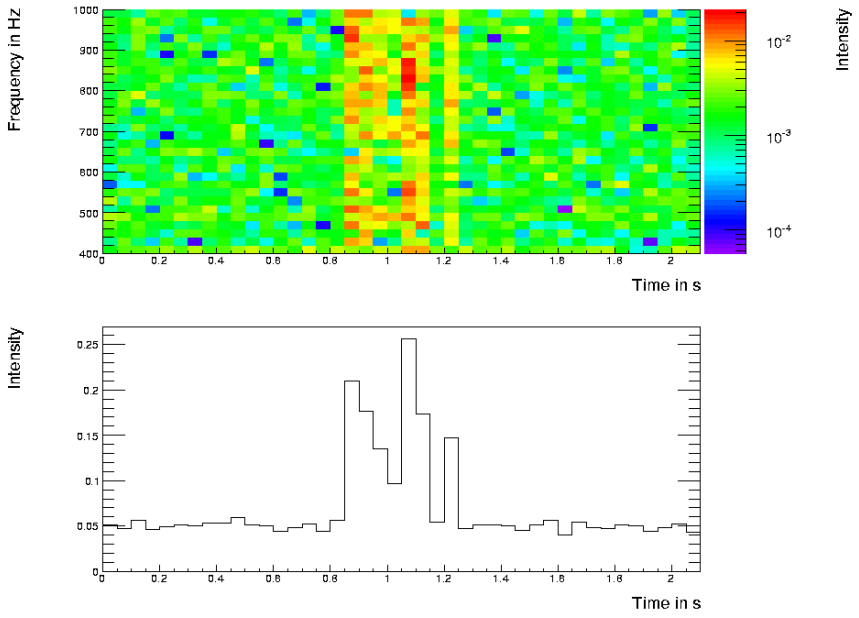

Figure 35: Signal found in the analysis. Because of frequency and intensity structure classified as broadband noise signal. Time resolution 0.05 s.

17.2. Variation of Counting Rate for whole Data Taking Period

Besides the shape analysis of individual events one can analyse the signal abundance as a function of time. It is shown in figure 36. It shows the variation of the number of received signals per day. Periods without entries are where the setup was inactive or the data files were rejected because of the activity of pulsed transmitters. The time of the maximum of the Perseid meteor shower is marked with two red lines. The time of the maximum of the Southern Delta Aquarids is marked with two blue lines. When we look

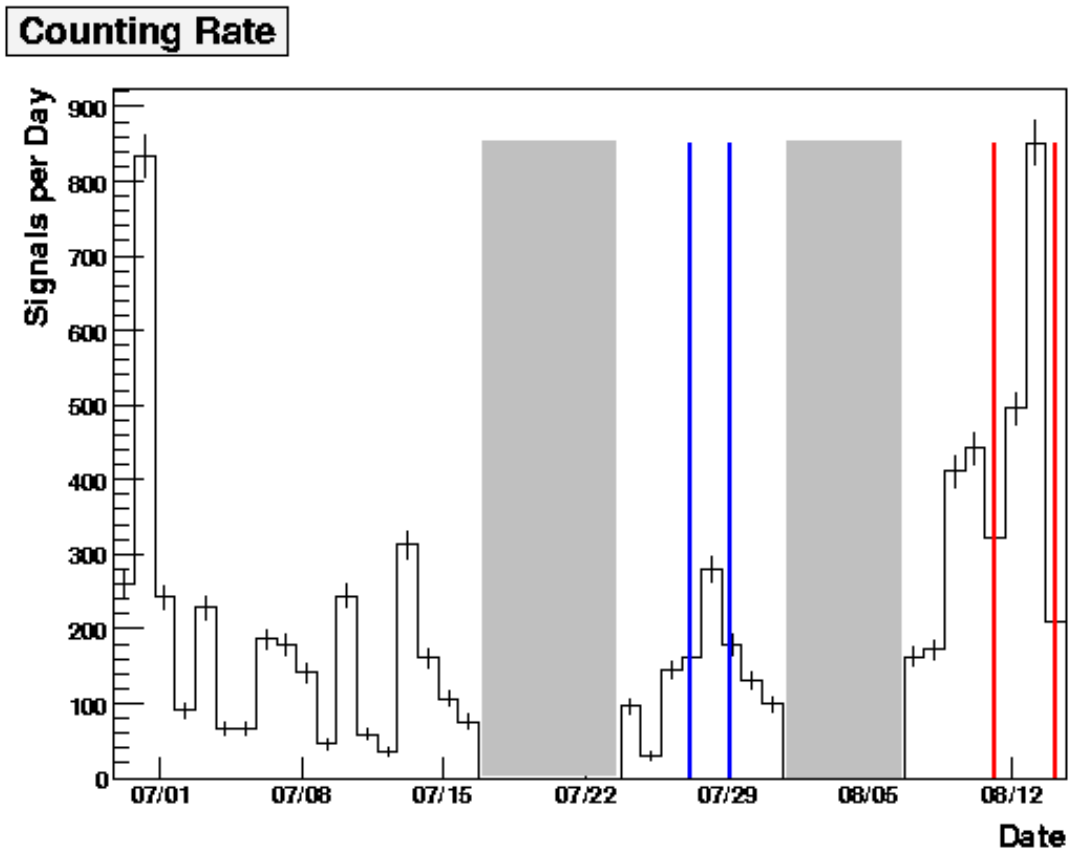

Figure 36: A Histogram showing the variation in counting rates per day for the whole data taking period. Shown on the x-axis is the the date and on the y-axis the number of signals per day. The peak time of two meteor showers is marked colored lines. Time periods without data are shaded in gray.

at the counting rates for the whole data taking period we see a massive rise in counting rates for the time of the Perseid maximum. The counting rates per day measured in this time are the highest in the whole data set. In addition the counting rates rise at the time of the maximum of the southern delta aquarids, but here a comparison is difficult because of setup downtime surrounding this date. The very high counting rates at the beginning of the data taking period do not coincide with any known meteor shower and are thus not explainable by regular shower activity. An eye scan of the detected signals

found a very high part of noise signals and signals that could not be classified. One possible explanation could be special atmospheric conditions that would generate the high number of noise or fake signals.

17.3. Signal Duration

The duration of the detected signals after the signal merging, here shown as the time dimension of the inner box is shown in figure 37. The minimum duration found is that of the dimension of the inner box, as expected. The duration with the highest number of signals is 0.3 s. The longest signal found had a duration of 9.1 seconds.

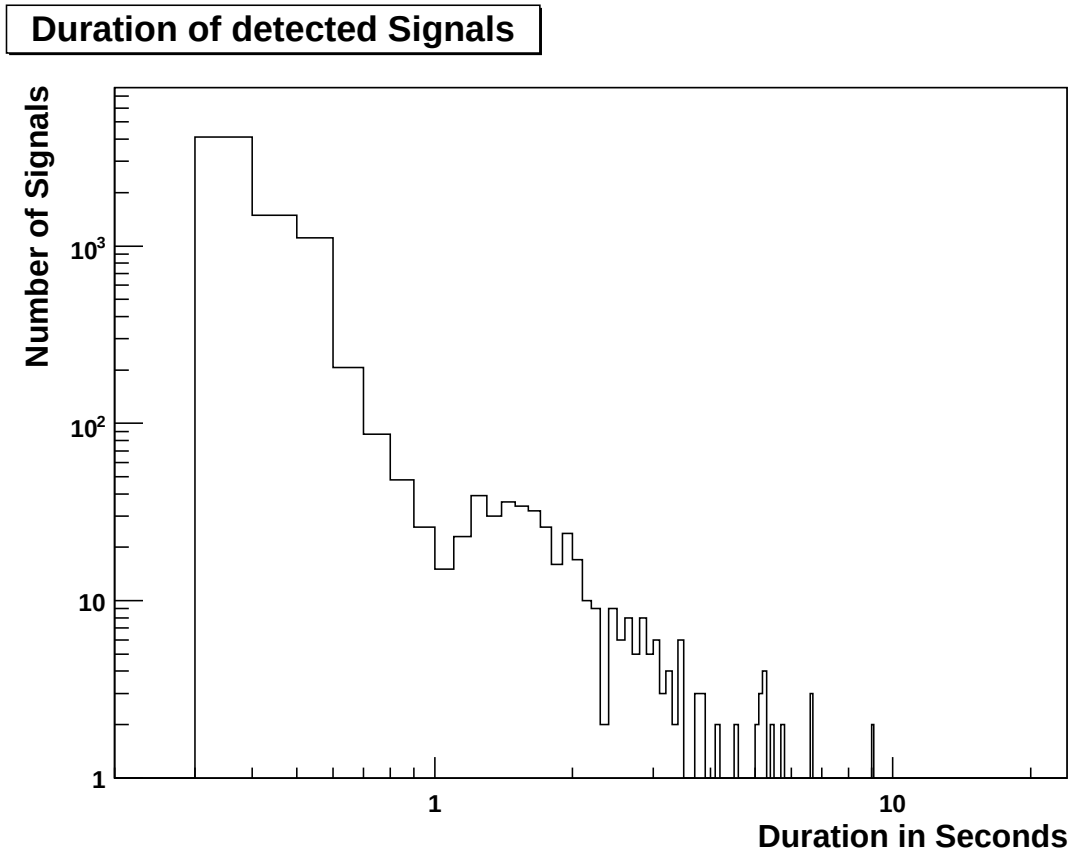

Figure 37: A Histogram showing the number of found signals against their duration. The minimal duration is that of the inner box with 0.3 s. The time resolution of the analysis was 0.1 s.

The distribution of signal durations is the same as that expected from meteor scatter signals. The duration of signals is roughly correlated with the initial ionisation density generated by the meteor. That density is again dependent on the mass of the meteoroid. In figure 10 in section 10 it was shown that the number of meteoroids entering the Earth's atmosphere growths with smaller size of the particles. That leads to higher rates of smaller meteors with smaller ionisation and in general shorter signal duration.

17.4. Time Difference between Signals

In figure 38 the time difference between subsequent signals is shown. The resulting curve looks like an exponential curve but is not fitable with a single function. A zoom in on the part with the smallest time differences in figure 39 shows that the curve does not continue to zero, but breaks somewhere between a time difference of one and two seconds. This can be explained by the limited time resolution and the signal merging in the analysis. Signals with a time difference smaller than 1.5 seconds would have been merged in the process. This leads to the low counts for the one to two seconds bin and the zero count for the zero seconds to one second bin.
A try to fit the resulting curve with a single exponential function has a very bad quality, resulting in a $\chi^2/Ndof$ of 2.216.

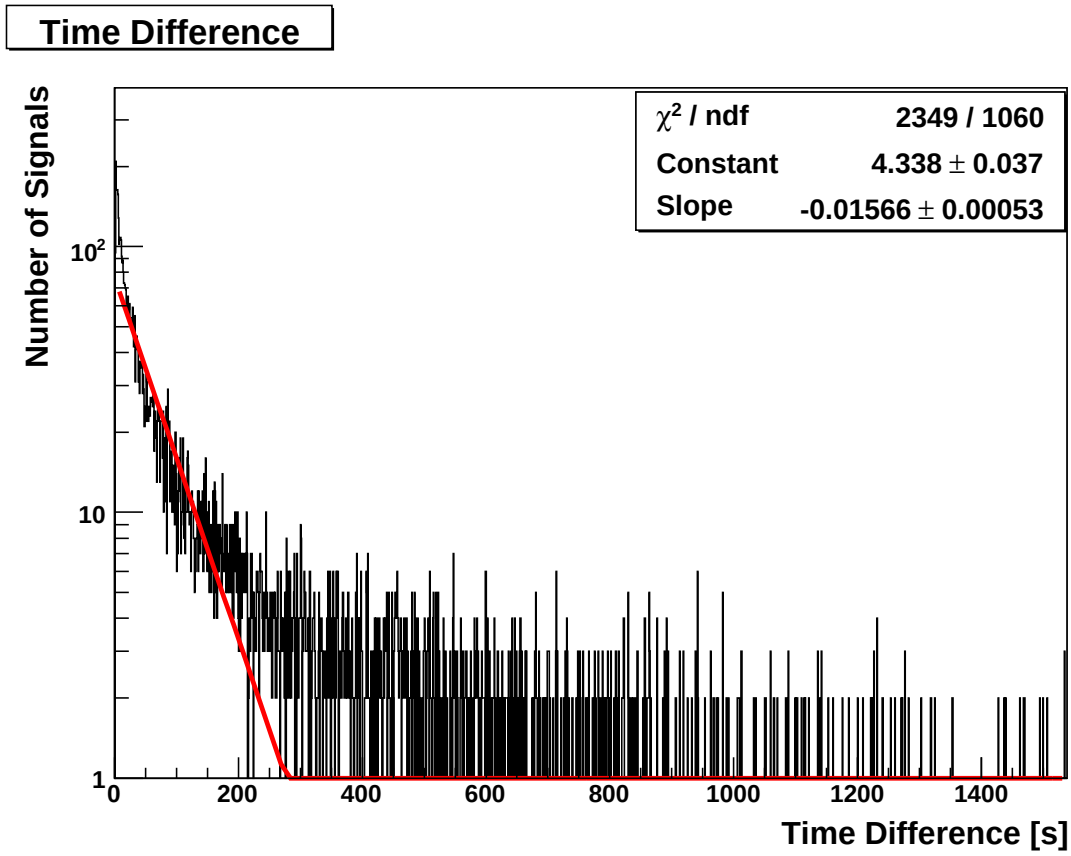

Figure 38: A Histogram showing the time difference between following signals. Shown on the x-Axis is the time difference and on the y-axis is the number of signals. An exponential fit to the data is shown in red.

If the found signals are statistically independent, as it is expected from meteor scatter signals and have a constant rate per time interval an exponential curve should be visible in the histogram. Man made signals are often periodic. They are not independent from each other and should lead to distinguished peaks in the histogram. In figure 36 we

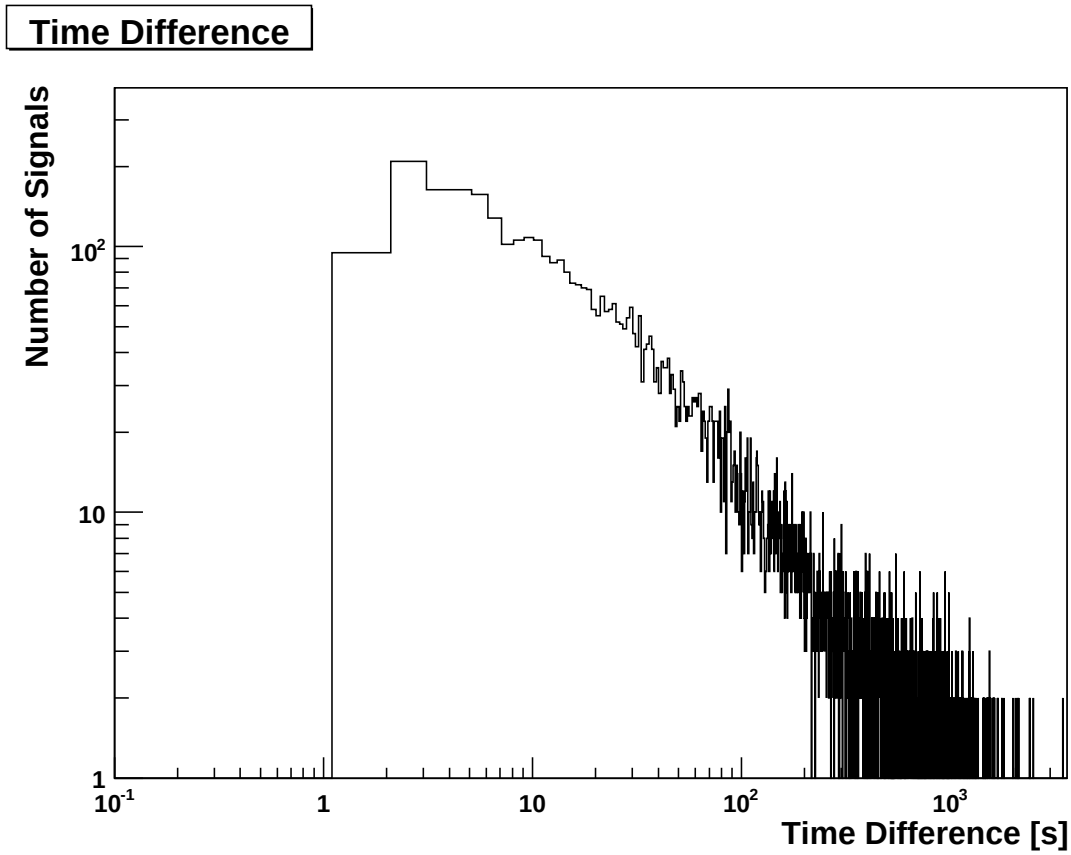

Figure 39: Double logarithmic plot of the time difference between signals shown in figure 38.

have seen that the counting rate is not constant but fluctuates strongly. That would lead to a superposition of several exponential functions. In figure 38 and 39 we see that the distribution looks like the combination of several exponential functions. We do not see isolated peaks that would show a regular dependence between the time differences. This leads us to the conclusion that the received signals are naturally occurring, statistically independent signals with changing counting rates per time as expected from meteor scatter signals.

17.5. Diurnal Variation of Counting Rate

The diurnal variation of counting rates is show in figure 40. Shown is the counting rate per hour for the whole data taking period. The x-axis shows the hours of the day in universal time, that is local time minus two hours for time periods with daylight saving time.

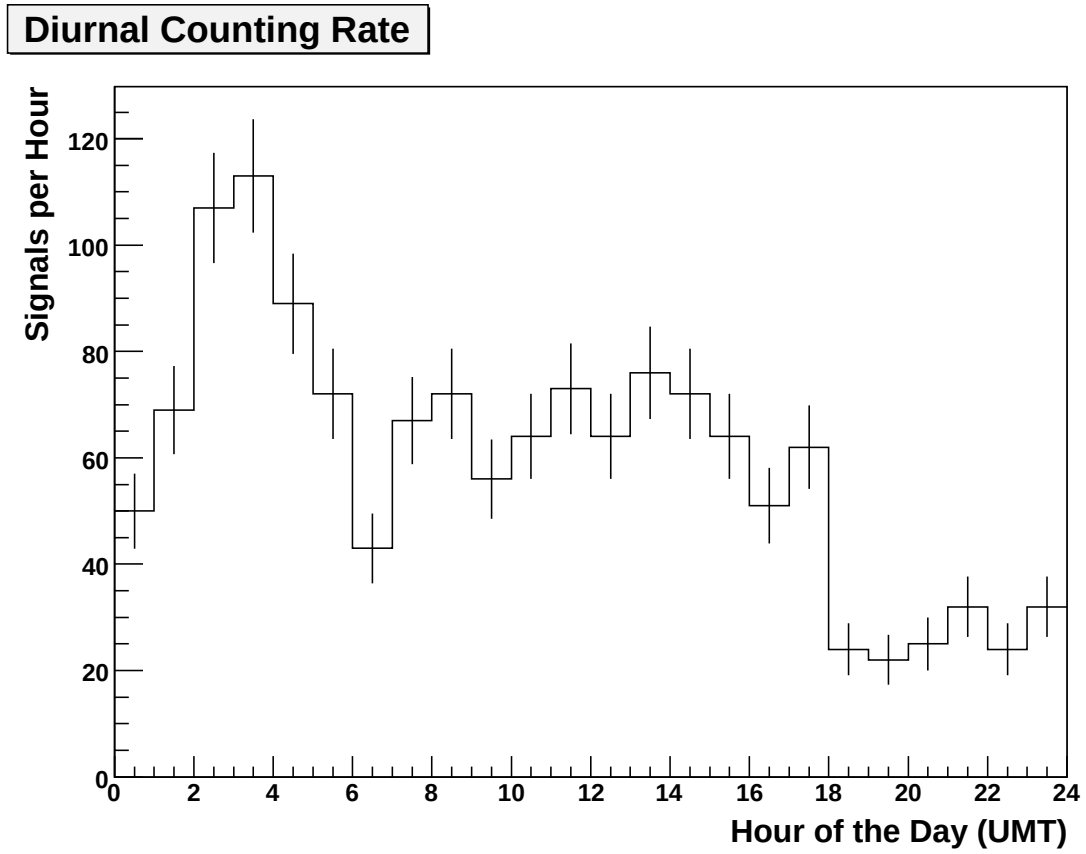

Figure 40: A Histogram showing the variation of counting rates per hour of the day for the whole data taking period. Shown on the x-axis is the time in universal time, that is local time minus two. Shown on the y-axis is the number of signals received per hour.

The possibly strongest hint for our hypothesis is the diurnal variation in counting rates. As shown in section 10.1 the counting rates of meteor scatter signals should change with the local time of the receiver. The highest rate should be achieved at the local time of sunrise and the lowest rate at the local time of sunset. For the time when the measurements were done sunrise was around 4 am local time, that is 02:00 universal time and sunset around 9 pm, that is 21:00 universal time. In figure 40 we see that the maximum and minimum rates occur at exactly these hours. The factor between maximum counting rates $R_{max} = 110/h \pm 10.5/h$ and minimum rates $R_{min} = 23/h \pm 4.8/h$ is $R_{max}/R_{min} = 4.8 \pm 1.5$, very close to the theoretical factor of 4, see section 10.1.

18. Measurements with rotated Antenna

An additional measurement done after these analyses was a measurement with a rotated antenna. That was to assure that the received signals were not generated somewhere close by and were indeed received long range signals. At first one day was measured with the antenna looking directly in the direction of the beacon. On the next day the antenna was turned by a large angle away from the beacon, after that one day of data was taken in the direction of the beacon and so on. Used angles were 90°, 180°and 270°. No known beacons with a frequency compatible with the antenna and a distance that would allow meteor scatter are in the field of view for these angles.
The result of these measurements was that only with the antenna looking in the direction of the beacon a high number of signals was detected. The rates for the other angles was much lower and the signals received do most of the time look like the signal in figure 35 that was classified as a noise signal. In addition only when looking at the beacon signals with an exponential intensity decay were found.
It follows that most of our received signals are long range signals originating at the distant beacon. An omnipresent noise background leads only to a small background in the counting rates.

19. Conclusion

From the results of the analysis done with our data we conclude that we have indeed measured meteor scatter signals. We don't have evidence supporting this hypothesis but several convincing hints. In addition many of the detected signals have an exponential decline in signal intensity. Examples are found in figure 33 and figure 34. This behavior stems from the exponential decay of the ionisation as expected from the theory. The combination of all these results leads us to the conclusion that the signals detected with our setup were radio signals generated by the beacon in Norway and scattered on ionisation trails produced by meteors in an altitude of around 90 km.
A final proof of this conclusion is not possible with our setup, but could be possible with an upgraded setup which would allow the triangulation of the scattering point or the coincident measurement of scatter signals with other detection concepts.

We showed that it is possible to detect very weak signals scattered on short lived ionisation columns generated by meteors in the high atmosphere. The used setup is very simple and relies on basic RADAR principles well understood. First hints that it is possible to measure the time development of the ionisation were found in our data. Listening to these signals leads to the assumption that many of the signals contain an inner structure in their intensity and frequency behavior. The timescales on which these structures occur is smaller than the resolution of our setup. A measurement with a setup

with higher time and frequency resolution would allow an analysis of this behavior and would possibly give information on the process of ionisation buildup, time development and the internal structure of the ionisation column. With this data information on the meteoroid and the atmosphere could be gained.

20. EAS Detection Possibilities

Our measurements show that the expected EAS signals would not be detectable by our used setup because of their much shorter lifetime and lower intensity. Equation 19 shows that the signal power and duration becomes larger for larger wavelengths/smaller frequencies. For EAS detection a compromise between larger noise background [1] and better signal quality has to be found. The possible frequency range is from 20 MHz to 60 MHz. In addition such measurements have to be far away from the man made noise of urban areas. The use of low frequencies results in the need for different antennas, receivers and amplifiers. In addition the data acquisition has to be upgraded: It must have a very small time resolution to allow the measurement of very short signals and their time development with great detail. A better frequency resolution of the setup would lead to the possibility to analyse the frequency substructure of the received signals and could lead to information on the ionisation production and decay. With this information additional information on the physics of air showers could be gained.

Another change of the setup is the different scatter geometry. Because of the much lower altitude of the ionisation columns of EAS than that of meteors the distance between receiver and transmitter has to be much smaller, somewhere between 30 kilometers and 100 kilometers. That limits the use of existing transmitters so that it will be necessary to build and use an own transmitter, or several with slightly different frequencies and locations, for the measurements. An additional benefit of the use of an active transmitter is the control over it, allowing the use of advanced RADAR techniques used in commercial and military RADAR applications.

When measurements of such an upgraded setup in coincidence with existing shower detectors allows the understanding of the RADAR signals, it is possible to extend the measurement capabilities of an EAS array by the use of an advanced multistatic RADAR setup. The expected capabilities of such a RADAR detector are:

- The possibility to measure the position and direction of the shower by triangulation with several transmitters and receivers in a multistatic RADAR setup.
- A measurement of the shower development for the whole length of the shower.
- A calorimetric measurement of the shower energy.
- Sensitivity to nearly horizontal showers that never reach the ground.
- The monitoring of a large part of the atmosphere surrounding the area monitored by the SD array with a high duty cycle leading to a high number of detected showers.

- The detection of neutrino induced air showers [36].
- Complementary measurements for existing air shower detectors.

Part VII.
Summary and Outlook

In this work a study on the feasibility of RADAR detection of extensive air showers was presented. RADAR detection in this context is the detection of radio waves scattered on ionisation columns produced by air showers.

It was shown that it is possible to build a functioning RADAR detector for scattered radio waves with off the shelf components for less than 1000 €. A first understanding of radio transmission, signal types and basic RADAR principles was achieved. With this detector it was possible to detect signals consistent with that expected from commercial airplanes and their Doppler shifts.

After little modification of the detector it was possible to detect radio waves scattered on ionisation columns generated by micro meteors. The distance between transmitter and receiver for this measurement was 811 km. It was possible to measure weak and short signals only somewhat longer than the expected lower boundary for signal duration from theoretical calculations. A diurnal variation in counting rates of the signals was found, leading to the conclusion that the process generating these signals depends on the local time of day, as expected from meteor scatter signals. The found signals occurred at random time intervals and were not generated by periodic man made processes. It was also possible to show that some signals have a time development as expected for ionisation columns. A large part of the detected signals was eye scanned and analysed by listening to them. An algorithm for the automatic detection of meteor scatter signals in data files was developed.

This measurements show that it is possible to use the RADAR principle for the study of ionisation columns. A next step towards the detection of EAS will be the measurement with several receiving antennas in coincidence with an existing EAS detector, for example the Pierre Auger Observatory in Argentina.

We see, that the detection of air showers with RADAR is a promising new detection concept. The production of ionisation columns is linked directly to the energy of the primary cosmic ray particle. RADAR detection has a nearly 100% duty cycle and is sensitive to the whole shower development.

The theoretical calculations for the production of ionisation columns and the scattering of ionisation columns are based on a approximations. The simulation of the ionisation columns generated by air showers and the scattering process without simplifying assumptions would lead to a better understanding of the detection possibilities. In addition a study of the atmospheric processes influencing the ionisation is needed for the simulation.

The RADAR detection alone could lead to high number of detected air showers because of the large monitored volume. The combination of SD and RADAR detection could result in complementary measurements of the shower parameters and in a high number of a different type of hybrid measurement when the FD is not operational. The combination of all three detection concepts could lead to a better understanding of the physics of air showers and cosmic rays.
Future updates to the used RADAR technology, today already used in airplane RADAR's, could allow an extension of the measurement capabilities of a possible RADAR detector, resulting in new research possibilities for extensive air showers.

Part VIII.
Appendix

21. Antenna Characteristics and Definitions

21.1. The Unit Decibel

A unit often used in audio and electronic science is the decibel. It is a logarithmic unit that describes a ratio and is used for power, sound pressure, voltage or intensity. It can be defined by the comparison of two identical loudspeakers that play the same sound, one with the power P_1 and the other with the higher power P_2. The difference in decibel for these two powers can then be given as:

$$10 \log \frac{P_2}{P_2} \; dB \tag{31}$$

If the second power was twice the power of the first the difference would be 3 dB. If the second power was one million times the first power the difference would be 60 dB. We see that with the decibel it is possible to show very small and very large ratios with small numbers. Because the dynamic range in sound or radio measurements can have such huge differences it is mostly used there.
Sometimes additional characters are added to the unit dB, for example dBi when antennas are compared to the ideal isotropic antenna.

21.2. Antenna Characteristics

The most important values to describe antennas are their bandwidth, their gain factor and their beamwidth. The bandwidth is described the easiest as frequency range in which the antenna is sensitive.

21.2.1. Gain Factor

To describe the effect that antennas have a directivity, meaning that they are more sensitive in a certain direction than in another the antenna gain is introduced. It describes for a given direction how much higher the received power is compared to a theoretical isotropic antenna. This value is given in dBi, with the index i showing that the isotropic antenna is the reference. Typical values for antennas are gain factors of G=5 dBi for low directivity antennas or higher for directional antennas. It follows that most antennas amplify the received signal compared to a isotropic antenna for a certain direction but are non sensitive for other areas [48].

21.2.2. Beamwidth

The beamwidth or 3 dB width of an antenna is the angle between the gain maximum of the antenna and the point where the gain factor is only half of the maximum value. It is used to give an idea of the sensitive area of an antenna [48].

22. Dimensions for the 2m Band Antenna

The 2 m band antenna consists of a 6.5 m long boom on which 13 parasitic elements, the receiving element and reflecting element are mounted. The boom is built from an aluminum beam and the elements are small aluminum strips mounted perpendicular to the boom. The dimension of the elements is shown in the following list.

Element	Type	Position	Length
1	Parasitic	2.5 cm	81.0 cm
2	Parasitic	54.0 cm	83.5 cm
3	Parasitic	104.5 cm	83.5 cm
4	Parasitic	155.5 cm	85.5 cm
5	Parasitic	207.5 cm	85.5 cm
6	Parasitic	259.0 cm	87.5 cm
7	Parasitic	309.5 cm	87.5 cm
8	Parasitic	361.5 cm	89.5 cm
9	Parasitic	412.5 cm	89.5 cm
10	Parasitic	464.0 cm	91.5 cm
11	Parasitic	516.0 cm	91.5 cm
12	Parasitic	567.0 cm	92.5 cm
13	Parasitic	596.0 cm	96.5 cm
14	Receiving	619.0 cm	97.5 cm
15	Reflecting	646.5 cm	109.0 cm

References

[1] T. Winchen. Measurements of the continuous radio background and comparison with simulated radio signals from cosmic ray air showers at the Pierre Auger Observatory - Diploma Thesis RWTH Aachen, 2007.

[2] P.M.S. Blackett and A.C.B Lovell. Radio echos and cosmic ray showers. *Proc. Roy. Soc. London*, A177:183, 1940.

[3] K. Suga. *Proc. Fith InterAmer. Seminar Cosmic Rays*, 2:XLIX, 1962.

[4] T. Matano et al. Tokyo large air shower project. *Can. Jour. Phys.*, 46:255, 1968.

[5] V. F. Hess. über Beobachtungen der durchdringenden Strahlung bei sieben Freiballonfahrten. *Physik. Zeitschr.*, XIII:1084, 1912.

[6] P. Auger, P. Ehrenfest, R. Maze, J. Daudin, and R. A. Fréon. Extensive cosmic-ray showers. *Rev. Mod. Phys.*, 11:288–291, 1939.

[7] D. J. Bird et al. *ApJ*, 424:491, 1994.

[8] E. Fermi. On the origin of the cosmic radiation. *Phys. Rev.*, 75:1169, 1949.

[9] T. K. Gaisser. *Cosmic Ray and Particle Physics*. Cambridge University Press, 1990.

[10] A. M. Hillas. The origin of ultra-high-energy cosmic rays. *Ann. Reo. Astron. Astrophys*, 22:425–444, 1984.

[11] The Pierre Auger Collaboration et al. Correlation of the highest-energy cosmic rays with nearby extragalactic objects. *Science*, 318:938, 2007.

[12] J. Cronin. International workshop on techniques to study cosmic rays with energies greater than 10^{19} eV - summary. *Nuclear Physics B - Proceedings Supplements*, 28:213, 1992.

[13] G. T. Zatsepin and V. Kuzmin. Upper limit on the spectrum of cosmic rays. *Sov. Phys. JETP Lett.*, 4:78, 1966.

[14] K. Greisen. End to the cosmic-ray spectrum? *Phys. Rev. Letters*, 16:748, 1966.

[15] J. Cronin, T. Gaisser, and S. Swordy. Cosmic rays at the energy frontier. *Scientific American*, 276:44, 1997.

[16] N. Hayashida et al. Observation of a very energetic cosmic ray well beyond the predicted 2.7 k cutoff in the primary energy spectrum,. *Phys. Rev. Lett.*, 73:3491, 1994.

[17] D. J. Bird et al. Evidence for correlated changes in the spectrum and composition of cosmic rays at extremely high energies. *Phys. Rev. Lett.*, 71:3401, 1993.

[18] M. Unger. Status und Ergebnisse des Pierre Auger Observatoriums. In *Gruppenvortrag auf der DPG Frühjahrstagung, Heidelberg*, 2007.

[19] K.-H. Kampert et al. Cosmic ray energy spectra and mass composition at the knee - recent results from KASKADE. *Nuclear Physics B (Proc. Suppl.)*, 136:273–281, 2004.

[20] H. Rebel A. Haungs and M. Roth. Energy spectrum and mass composition of high-energy cosmic rays. *Reports on Progress in Physics*, 66:1145, 2003.

[21] T.Yamamoto for the Pierre Auger Collaboration. The UHECR spectrum measured at the Pierre Auger Observatory and its astrophysical implications. In *Proceedings of the 30th International Cosmic Ray Conference - ICRC'07*, 2007.

[22] S. Eidelman et al. Review of particle physics. *Physics Letters B*, 592:1, 2004.

[23] J. Cronin. The highest-energy cosmic rays. *arXiv:astro-ph/0402487 v1*, 2004.

[24] T. K. Gaisser and A. M. Hillas. *Proc. 15th Int. Cosmic Ray Conf. (Plovdid)*, 8:353, 1977.

[25] J. Nishimura. *Prog. Cosmic ray Physics vol III.* North Holland, Amsterdam, 1956.

[26] K. Kamata and J. Nishimura. *Prog. Theor. Phys. Suppl.*, 6:93, 1958.

[27] K. Greisen. *Prog. Cosmic ray Physics vol III.* North Holland, Amsterdam, 1956.

[28] The Auger Collaboration. The Pierre Auger Observatory - Design Report. Technical report.

[29] P. Mantsch for the Pierre Auger Collaboration. The Pierre Auger Observatory - progress and first results. *arXiv:astro-ph/0604114v1*, 2005.

[30] T.Waldenmaier et al. Measurement of the fluorescence yield in air with the AirLight experiment. In *Proc. 29th Int. Cosm. Ray Conf., Pune, India*, 2005.

[31] R. Knapik, P. Bauleo, B.R. Becker, J. Brack, R. Caruso, C. Delle Fratte, A. Dorofeev, J. Harton, A. Insolia, J.A.J. Matthews, A. Menshikov, F. Ortolani, P. Petrinca, A. Pichel, S. Riggi, M. Roberts, J. Rodriguez Martino, A.C. Rovero, M. Scuderi, A. Tamashiro, D. Torresi, V. Tuci, and L. Wiencke for the Pierre Auger Collaboration. The absolute, relative and multi-wavelength calibration of the pierre auger observatory fluorescence detectors. *Proceedings of the 30th International Cosmic Ray Conference*, 2007.

[32] The Auger Collaboration. Properties and performance of the prototype instrument for the Pierre Auger Observatory. *Nuclear Instruments and Methods in Physics Research A*, 523:50–95, 2004.

[33] N. J. Willis. *Bistatic Radar.* Artech House Inc., 1991.

[34] M. H. Carpentier. *Principles of Modern Radar Systems*. Artech House Inc., 1988.

[35] A. Ludloff. *Praxiswissen Radar und Radarsignalverarbeitung*. Vieweg Verlag, 1998.

[36] P. W. Gorham. On the possibility of radar echo detection of ultra-high energy cosmic ray- and neutrino-induced extensive air showers. *arXiv:hep-ex/0001041 v3*, 2000.

[37] Z. CEPLECHA, J. BOROVIČKA, W. G. ELFORD, D. O. REVELLE, R. L. HAWKES, V. PORUBČAN, and M. ŠIMEK. Meteor phenomena and bodies. *Space Science Reviews*, 84:327–471, 1998.

[38] I.A. Glover. Meteor burst propagation. *Electronics & Communication Engineering Journal*, August:185–192, 1991.

[39] D. W. R. McKinley. *Meteor Science and Engineering*. McGraw Hill, New York, 1961.

[40] Jacob Z. Schanker. *Meteor Burst Communications*. Artech House Inc., 1990.

[41] S. Nedeljkovic and C.B. Netterfield. Forward scattering of meteors at multiple frequencies. *Publ. Astron. Obs. Belgrade*, 80:179–184, 2006.

[42] J. Jones and W. Jones. Oblique-scatter of radio waves from meteor trains: Long wavelength approximation. *Planet. Space Sci.*, 38:925–932, 1990.

[43] J. Jones and W. Jones. Oblique-scatter of radio waves from meteor trains: Full-wave calculations. *Planet. Space Sci.*, 39:1289–1296, 1991.

[44] J. Jones and W. Jones. Oblique-scatter of radio waves from meteor trains: Theory. *Planet. Space Sci.*, 38:55–66, 1990.

[45] THE LOPES COLLABORATION. Advanced detection methods of radio signals from cosmic rays for KASCADE GRANDE and Auger. In *Acoustic and Radio EeV Neutrino Detection Activities: Proceedings of the International Workshop (ARENA 2005)*, 2006.

[46] The Root Team. Root. http://root.cern.ch.

[47] B. Klingen. *Fouriertransformation für Ingenieur- und Naturwissenschaften*. Springer Verlag, 2001.

[48] Karl Rothammel. *Rothammels Antennenbuch*. DARC Verlag Baunatal, 2002.

[49] U. Hacker. Private communication.

[50] Magazin für Amateurfunk auf VHF, UHF & SHF. www.dubus.de, 2007.

[51] Google. Google earth viewer. http://earth.google.com/.

[52] N. Hansen. Private communication.

Acknowledgments - Danksagung

Für die Möglichkeit ein interessantes Thema im aktuellen Gebiet der Teilchenastrophysik zu bearbeiten danke ich Professor Thomas Hebbeker. Für die angenehme Betreuung meiner Diplomarbeit und viele anregende Diskussionen danke ich Matthias Leuthold. Professer Martin Erdmann und Professor Thomas Hebbeker danke ich für die Möglichkeit das Experiment in Argentinien zu besichtigen.

Für unzählige Hilfestellungen, Diskussionen und Anregegungen in der täglichen Arbeit danke ich Hans Dembinski, Tobias Winchen und Stefan Fliescher.

Für die Unterstützung bei Aufbau und Inbetriebnahme des Setups danke ich der mechanischen und elektrischen Werkstatt des III. Physikalischen Instituts der RWTH Aachen.

Ich danke auch dem DARC (Deutscher Amateur-Radio-Club e.V.) Ortsverband G01 Aachen und ganz besonders Herrn Uli Hacker - DK2BJ, ohne dessen Unterstützung durch Hardware-Leihgaben und intensive Diskussionen große Teile dieser Arbeit nicht möglich gewesen wären.

Als letztes danke ich der Person, ohne deren andauernde Unterstützung mein Studium nicht möglich gewesen wäre: Meinem Vater, Klaus Scharf.

Erklärung

Hiermit versichere ich, daß ich diese Arbeit einschließlich evtl. beigefügter Zeichnungen, Kartenskizzen u.ä.m. selbständig angefertigt und keine anderen als die angegebenen Hilfsmittel und Quellen benutzt habe. Alle Stellen, die dem Wortlaut oder dem Sinn nach anderen Werken entnommen sind, habe ich in jedem einzelnen Fall unter genauer Angabe der Quelle deutlich als Entlehnung kenntlich gemacht.

Nils Scharf, Aachen den 20. Februar 2008